POLITECNICO DI MILANO

Facoltà di Ingegneria Industriale

Corso di Laurea
in Ingegneria Aeronautica

Radial Fingering in a Hele-Shaw cell

Relatore: Prof. Maurizio Quadrio
Correlatore: Prof. Peter J. Schmid

Tesi di Laurea di:
Marco Nicotra 751951

ANNO ACCADEMICO 2010-2011

Marco Nicotra: *Radial Fingering in a Hele-Shaw cell,* MSc Thesis, 2012, March.

E-MAIL:
marco1.nicotra@mail.polimi.it

ABSTRACT

In this document, the dynamics of an interface under the influence of surface tension is studied numerically for the flow in a Hele-Shaw cell, where the interface separates an expanding bubble of a low viscosity fluid from a displaced high viscosity fluid. This flow highlights the phenomenon of viscous fingering. The flow field is discretized by a finite differences approximation, and the interface is explicitly represented by a separate, unstructured grid that moves through the stationary grid. In addition to keeping the viscosity stratification sharp, the tracked interface provides a natural way to include surface tension effects. A level contour reconstruction technique enables to naturally, automatically and robustly model the merging and breakup of interfaces. The effect of a mass inflow composed by a static part and a superimposed armonic component is investigated in order to find out effectives techniques for the reduction of the fingering effect.

KEY WORDS Viscous fingering, Hele-Shaw cell, oil recovery, multiphase flow, front tracking, topology change, surface tension

SINTESI

Con il termine *viscous fingering* ci si riferisce alla nascita ed all'evoluzione di instabilità all'interfaccia tra due fluidi in un mezzo poroso.
Flussi bifase in mezzi porosi sono caratteristici di numerosi casi di interesse pratico, tra cui quello più importante è certamente il processo di estrazione del petrolio.

Viscous fingering ed ingegneria petrolifera

Generalmente il petrolio si trova nel sottosuolo, intrappolato nelle cosiddette rocce serbatoio (*reservoir*), ovvero rocce di origine sedimentaria caratterizzate da alta porosità e permeabilità.
L'estrazione può avvenire in modo naturale se la pressione nel sottosuolo è sufficiente a spingere il greggio dal giacimento al pozzo petrolifero in superficie (questa prima fase è denominata "coltivazione primaria"). Tuttavia durante il processo di estrazione la pressione nel serbatoio diminuisce rapidamente, esaurendo il flusso di greggio verso la superficie.
L'iniezione di un secondo fluido nel sottosuolo (acqua o anidride carbonica) allo scopo di ritardare la depressurizzazione, permette l'estrazione di ulteriore greggio. Durante queste operazioni ("coltivazione secondaria") tuttavia si sviluppa un'instabilità idrodinamica all'interfaccia tra il greggio ed il secondo fluido. Questa instabilità nasce quando un fluido poco viscoso (acqua o anidride carbonica) ne spinge uno più viscoso (petrolio) in un mezzo poroso.
Il risultato di questo meccanismo è che il fluido meno viscoso penetra nella zona occupata da quello più viscoso formando strutture elongate a forma di dita, da cui il nome *viscous fingering* (figura 1).
Lo svilupparsi di queste strutture è dannoso dal punto di vista del-

Figura 1: *Viscous fingering* dovuto all'iniezione di cherosene in olio minerale [9]

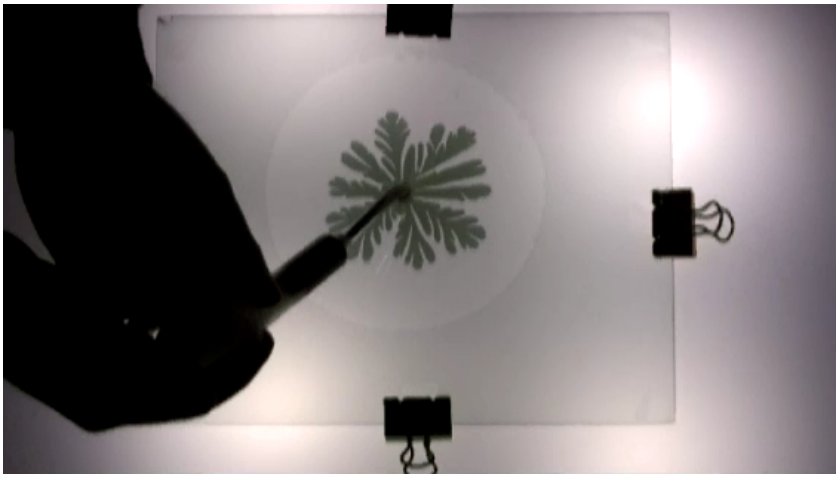

Figura 2: Set-up sperimentale: cella di Hele-Shaw

l'efficienza della tecnica di estrazione in quanto le "dita" raggiungono rapidamente i punti di estrazione "cortocircuitando" il flusso di petrolio e limitandone quindi la quantità che si riesce ad estrarre.

I primi studi

Nel 1956 Geoffrey Taylor visitò una piccola compagnia petrolifera Texana, la "Humble Oil Company" ed iniziò ad interessarsi al problema. Egli scrisse, insieme a P. G. Saffman, un primo articolo sull'argomento, in cui considerarono un problema modello: il flusso di Hele-Shaw. Siccome fare esperimenti su flussi in mezzi porosi è molto difficile in quanto, non essendo trasparenti, non si possono effettuare visualizzazioni, Saffman e Taylor studiarono l'instabilità all'interfaccia tra due fluidi all'interno di un sistema costituito da due piastre di vetro separate da un piccolo spazio di larghezza b, ovvero la cella di Hele-Shaw. Questo set-up (figura 2) permette di modellare il flusso in un mezzo poroso in quanto la stessa equazione (*Darcy's law*) governa la relazione tra velocità e pressione: la velocità media del fluido è in entrambi i casi proporzionale al gradiente di pressione, diviso per la viscosità μ. La costante di proporzionalità è nel caso del mezzo poroso (meno) la sua permeabilità e nel caso della cella di Hele-Shaw $-b^2/12$.

Da allora questa instabilità è nota con il nome di instabilità di Saffman-Taylor. Grazie alla sua semplicità ed alle potenziali applicazioni ha ricevuto grandi attenzioni dalla comunità scientifica come archetipo per sistemi caratterizzati dalla formazione di *patterns*.

Esistono due tipi di instabilità di interfaccia in una cella di Hele-Shaw: nel caso in cui un fluido più pesante stia sopra ad uno più leggero in presenza di gravità e con interfaccia inizialmente rettilinea (figura 3) e nel caso in cui un fluido meno viscoso sia pompato in un fluido più viscoso (geometria radiale). Quest'ultimo caso è quello più rappresentativo per quanto riguarda l'applicazione petrolifera: l'acqua (o l'anidride carbonica) è pompata da punti di immissione che sono a tut-

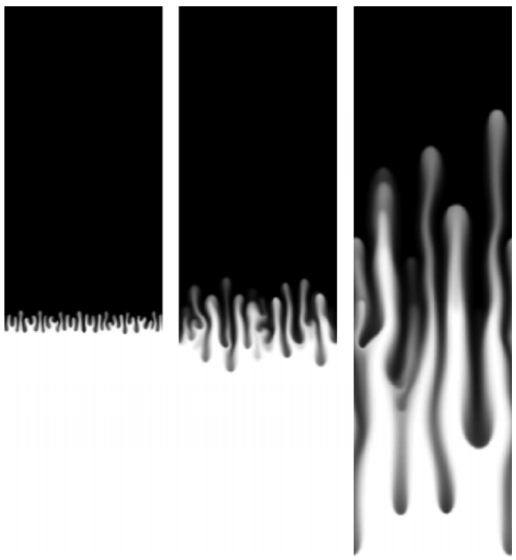

Figura 3: Instabilità gravitazionale: simulazione numerica di Trevelyan, Almarcha e de Wit [28]

ti gli effetti sorgenti puntuali e lo spostamento (quantomeno all'inizio) è quindi in direzione radiale.
Il fenomeno del *viscous fingering* è stato studiato molto negli ultimi decenni, sia tramite esperimenti che per mezzo di simulazioni numeriche (consultare le *reviews* di Homsy [13] e Bensimon et al. [5]). La parte più consistente della produzione scientifica è basata sulla soluzione di equazioni integrali di contorno, grazie alle quali si può ridurre la dinamica del sistema a quella della sola interfaccia che separa i due fluidi o le due fasi (consultare Hou, Lowengrub e Shelley [14]).

Il controllo del viscous fingering

Sono stati inoltre fatti molti tentativi di quantificare da un punto di vista fluidodinamico l'efficacia di varie tecniche di controllo atte a ridurre l'effetto del *fingering*.
Anke et al. [2], nei loro esperimenti, investigarono come va a modificarsi l'instabilità di Saffman-Taylor quando si utilizzano fluidi complessi, quali possono essere soluzioni diluite di surfactanti e/o di polimeri. I surfactanti permettono di modificare la tensione superficiale, mentre i polimeri influenzano l'azione viscosa. Essi verificarono che l'instabilità di Saffman-Taylor è modificata drasticamente dalle proprietà di fluidi complessi e che ciò può essere sfruttato per ottenere un miglior spostamento del greggio nel giacimento, migliorando così l'efficienza del processo di estrazione.
Li et al. [20], controllando la portata di fluido immessa, cercarono (sperimentalmente e numericamente) di sopprimere l'evoluzione dell'instabilità interfacciale. Essi suggerirono che, se la portata immessa è scalata con il tempo come $t^{-1/3}$, può essere possibile ottenere una crescita si-

milare delle dita, evitando quindi regimi con pattern molto complessi.

Obiettivo della tesi

Lo scopo di questo lavoro è quello di produrre uno strumento operativo efficiente per simulare il *viscous fingering* in geometria radiale e per studiare l'efficacia di eventuali tecniche atte al suo controllo. In particolare si vuole studiare la possibilità di sopprimere selettivamente alcune strutture instabili in modo da ridurre l'estensione del fingering. A questo scopo simuliamo la risposta del sistema ad un forzamento non stazionario (in termini di portata di fluido immessa), composto da una parte statica e da una componente armonica sovrapposta. La speranza è quella che, per alcune combinazioni di ampiezza e frequenza della parte armonica del forzamento, la crescita delle strutture interfacciali sia smorzata e l'estensione del *fingering* ridotta.

Sotto l'effetto combinato di pompaggio ed aspirazione ci si aspetta che l'interfaccia possa rompersi, portando al distacco di bolle, e/o alla fusione di strutture distinte.

Cambi di topologia

Di conseguenza il nostro metodo deve essere in grado di gestire cambi di topologia del contorno tra le due fasi.

Quando l'interfaccia è tracciata esplicitamente per mezzo di punti connessi tra loro (*Tracking methods*, come i metodi a vortici ed i metodi *Contour dynamics*[1]) questi cambi di topologia vanno accompagnati ad un cambio appropriato nella connettività di questi punti. La complessità di questa operazione è considerata il maggior svantaggio di questi metodi.

Nei metodi che seguono il contorno tra fasi tramite una appropriata funzione continua (*Capturing methods*, come i metodi *Volume of fluid* e *Level set*[2]) il cambio di topologia avviene automaticamente quando due interfacce o due parti della stessa interfaccia arrivano ad essere distanti meno di una o due spaziature di griglia. Questa coalescenza automatica può essere molto conveniente, specialmente se il cambio di topologia non deve essere trattato con particolare accuratezza, ma può essere anche un punto di debolezza del metodo numerico.

Il metodo descritto in questo lavoro è una specializzazione del metodo derivato da Shin e Juric [26], un ibrido tra una tecnica *front capturing* e *front tracking*. Esso fa uso di una griglia cartesiana stazionaria per il flusso, mentre l'interfaccia è tracciata per mezzo di una griglia separata di dimensione inferiore. Tuttavia, al contrario dei metodi *Front tracking*, dove ciascuna fase è considerata separatamente, qui tutto il campo di moto è risolto per mezzo di un singolo set di equazioni di governo.

I cambi di topologia sono modellati in modo molto robusto grazie ad una tecnica di ricostruzione dell'interfaccia, intesa come una particolare linea di livello di una funzione continua. Grazie a questa procedura gli elementi che costituiscono l'interfaccia sono fisicamente connessi,

1 Vedere rispettivamente Cottet e Komoutsakos [7] e Zabusky, Hughes e Roberts [33]

2 Vedere rispettivamente Hirt e Nichols [12] e Sethian [25]

ma non logicamente, semplificandone notevolmente il *tracking* lagrangiano.

Il documento è strutturato come segue:

Struttura del documento

1. **INTRODUZIONE**

2. **PETROLIO, VISCOUS FINGERING E FLUSSO DI HELE–SHAW** Si fornisce una breve introduzione all'importanza del *viscous fingering* come archetipo per sistemi soggeti allo sviluppo di *patterns*. Sono spiegate le principali caratteristiche di non linearità, non località e mescolamento. A seguire si trova una breve digressione riguardante le tecniche utilizzare per migliorare l'efficienza delle tecniche di estrazione del petrolio relativamente al fenomeno del *viscous fingering*. Il modello fisico del flusso di Hele-Shaw è analizzato in dettaglio, anche grazie ad un'analisi linearizzata che permette di capire il meccanismo di crescita che governa il fenomeno.

3. **FORMULAZIONE MATEMATICA** Si ricavano le equazioni di governo del flusso di Hele-Shaw a partire dalle equazioni di Navier-Stokes per flussi incomprimibili multifase. Si ricava anche una forma adimensionale di queste equazioni mettendo in evidenza l'effeto dei diversi parametri adimensionali che governano il fenomeno.

4. **METODO NUMERICO** Si descrive il metodo numerico, con particolare attenzione al trattamento della tensione superficiale ed alla procedura di ricostruzione dell'interfaccia in relazione ai cambi di tipologia. Si introduce la funzione di distribuzione di Peskin per il trasferimento delle informazioni dalla griglia stazionaria all'interfaccia.

5. **ESPERIMENTI NUMERICI** Il codice è validato tramite confronto con i risultati analitici della teoria linearizzata. Si presentano dei risultati significativi di simulazioni numeriche in entrambi i casi di forzamento stazionario e non.

6. **CONCLUSIONI**

7. **APPENDICI**

ACKNOWLEDGEMENTS

I don't want to achieve immortality through my work. I want to achieve it through not dying.

Woody Allen

I would like to express my gratitude to the *Laboratoire d'Hydrodynamique* (*LadHyX*) of the École Polytechnique, Paris, for their hospitality during the months of October, November and December 2011. In particular I would like to thank Prof. Peter Schmid, whose fatherly encouragement and support enabled me to carry out this thesis.
I owe my deepest gratitude to Prof. Maurizio Quadrio, who gave me the unique possibility to experience life abroad, putting his confidence in me and granting me a lot of his time.
I am also grateful to Fulvio Martinelli for the friendly help he gave me and for all his sound advices[3].
Lastly, a special thanks go to Marco Carini, who gave me his unselfish support in Paris.

Vorrei poi ringraziare tutti coloro che mi hanno accompagnato nel viaggio in questa Sparta dello studio che è il Politecnico di Milano. I professori che in questi anni mi hanno comunicato qualcosa, che siano stati insegnamenti o semplici regole di vita, ed anche chi, nel suo modo tutto particolare, mi ha insegnato che nella vita non si smette mai di imparare[4].
Ringrazio l'ormai canadese Andre, socio di "picchi" e grande amico, il Caga®, compagno inseparabile dei primi anni, il Sarti, per tutti gli "sbatti" lanciati e per le cosiddette "*connection* vincenti", e tutti i compagni con cui ho condiviso qualcosa in questi anni, che siano pranzi alla Svolta®, cene al Kapuziner, attese infinite fuori dal Dipartimento prima di un esame o partite a calcetto . *I wish you the best*.

Dulcis in fundo. Il grazie più grande va alla mia famiglia. A papà Vincenzo, un ingegnere con il camice e lo stetoscopio, che giustamente ancora si chiede come abbia fatto a passare tanti esami senza tuttora essere capace di piantare un chiodo. A mamma Paola ed a mia sorella

3 *«Mai mollare!»*
4 *«Ma lei l'ha letto il Bisplinghoff?»*

Silvia, per aver cercato di fare in modo che la deriva ingegneristica non prendesse il sopravvento su di me. È anche grazie a voi se ancora non indosso polo abbottonate fino all'ultimo bottone.
Il ringraziamento più dolce va a te Marta, per aver condiviso ogni fatica ed ogni successo, ogni «*Devo studiare*» ed anche un «*Mi sono dimenticato la macchina a Milano*»; insomma per aver sopportato uno studente di ingegneria un po' particolare, con tutto quello che comporta. So che l'hai fatto con tutto l'amore possibile. Grazie.

Ma adesso andiamo a festeggiare!

Milano, 23 Marzo 2012

Marco Nicotra

CONTENTS

LIST OF FIGURES

1 INTRODUCTION

Two-phase flow in porous media occurs in a large number of practical situations, arguably the most important of which is oil recovery.
Petroleum is generally found in porous rocks; the crude oil can be extracted from a well because it is pushed out by the high pressure in the reservoir. However, in the process of recovery the pressure decreases rapidly and the oil flow stops. Injection of another fluid (water or carbon dioxide gas injected below or above the oil layer respectively) allows extracting more oil from the well.
In such water-flooding operations, however, an hydrodynamic instability can develop at the interface between the water and the crude oil. This instability arises when a less viscous fluid (water or gas) pushes a more viscous one (oil) in a porous medium. As a result of the instability, "fingers" of the less viscous fluid grow in the more viscous one. These fingers become narrower as the flow through the reservoir increases.
This instability limits the output of a well, because if the flux becomes too high, the fingers may reach the entrance of the well rapidly, and mainly water or gas instead of oil will be recovered.
In 1956 Sir Geoffrey Taylor visited a small oil company called the "Humble Oil Company" and became interested in this problem. In a seminal paper [24], written jointly with P.G. Saffman, they considered an idealised version of the problem. As experiments in porous media are not easy, since they are not transparent, Taylor studied the interfacial instability of a two-phase flow in a Hele-Shaw cell: two parallel glass plates separated by a small gap b. Such a set-up models the flow in a porous medium: the same equation (Darcy's law) determines the relation between velocity and pressure gradient in both porous media and the Hele-Shaw cell. The average velocity of the fluid is proportional to the pressure gradient over the viscosity μ. The coefficient of proportionality is (minus) the permeability for the porous medium and $-b^2/12$ in the Hele-Shaw cell.

The very first studies

Indeed, in the Hele-Shaw cell the formation of "fingers" of the less viscous fluid into the more viscous fluid was observed. Ever since, this instability has been known as the Saffman-Taylor (or viscous fingering) instability. Because of its relative simplicity, and its potential applications, it has received much attention and has become an archetype of pattern-forming systems.

An interface in a Hele-Shaw cell can be unstable for two reasons. If a heavier fluid is on top of a lighter one, the interface is gravitationally unstable. If, owing to pumping, a less viscous fluid is made to displace a more viscous one, the interface is also unstable.

In practice, when fluids are injected into the ground, they are injected through a well which, in effect, is a point source. Displacement (initially at least) is in the radial direction. One would therefore consider the radial model to be more appropriate to practical situations than the linear displacement model.

The viscous fingering phenomena has been intesively studied in the past, both through laboratory experiments and numerical simulations, to explain the onset and growth of the instabilities (see reviews in Homsy [13] and Bensimon et al. [5]). Most of the scientific production on the numerical simulation of the Hele-Shaw flow is based on the application of boundary integral methods, thanks to whom the dynamics of the system can be reduced to the self-contained, nonlocal dynamics of the interface separating the homogeneous fluids or phases (see a review in Hou, Lowengrub, and Shelley [14]).

A number of attempts have been made to quantify, from a fluid dynamic point of view, the effectiveness of various techniques apt to reduce the fingering effect.

Controlling the fingering

Anke et al. [2], in their experiments, probed the modification of the Saffman-Taylor instability when so called complex fluids are used, which are diluite solutions of surfactants and/or polymers. Surfactants allow one to modify the capillary forces while polymers affect the viscous forces; these are the two forces governing the instability. They (and many others) discovered that the Saffman-Taylor instability is drastically modified by the properties of complex fluids and that this can lead to a more efficient displacement of the crude oil in the reservoir, and should thus improve recovery rates.

Li et al. [20] studied numerically and experimentally the dynamics and control of viscous fingering patterns in a circular Hele-Shaw cell. By controlling the injection rate of the less viscous fluid thet tried to suppress the evolving interfacial instabilities. They suggested that if the injection rate scales with time like $t^{-1/3}$ it may be possible to obtain self-similar growing fingers, thus avoiding the dense-branching morphology regime. Their experiments confirmed the feasibility of the control strategy.

Purpose of the current work

The aim of this work is to create an effective tool to simulate viscous fingering in a radial geometry and to study the effectiveness of its control. In particular we want to investigate the possibility of selectively suppressing some unstable structures in order to reduce the extent of the fingering.

To this aim we simulate the response of the system to an unsteady

forcing (mass inflow) composed by a static part and a superimposed armonic component. A number of simulations in a broad band of frequencies and amplitudes are carried out.
We hope that for certain combinations of frequencies and amplitudes of the armonic part of the forcing, the growth of the interface perturbations is dumped and the extent of fingering reduced.
Under the alternate effect of suction and pumping we expect the interface to eventually break up, causing the pinching of fingers into droplets or the merging of different sections of the interface.

Topology changes

Consequently our method must account for topology changes of the phase boundary.
When the interface is explicitly tracked by connected marker points (*Tracking methods*, such as *Vortex method* and *Contour dynamics method*[1]), such changes must be accounted for by changing the connectivity of the points in the appropriate way. The complexity of this operation is often cited as the greatest disadvantage of front tracking methods.
In methods that follow the phase boundaries by a marker function (*Capturing methods*, such as *Volume of fluid method* and *Level set method*[2]), topology changes take place whenever two interfaces, or different parts of the same interface, come closer than about one grid spacing. While automatic coalescence can be very convenient in some cases, particularly if the topology change does not need to be treated accurately, this can be also a serious weakness of such methods.
The method described in this work is a specialization of the method derived by Shin and Juric [26]. This method is a hybrid between a front capturing and a front tracking technique. A stationary regular grid is used for the fluid flow, but the interface is tracked by a separate grid of lower dimension. However, unlike front tracking methods where each phase is treated separately, all phases are treated together by solving a single set of governing equations for the whole flow field.
The merging and breakup of interfaces are robustly modeled thanks to a level contour reconstruction technique in which the surface elements are physically linked but not logically connected, simplifying the Lagrangian tracking.

Structure of this document

This document is structured as follows:

1. **INTRODUCTION**

2. **OIL RECOVERY, VISCOUS FINGERING AND THE HELE–SHAW FLOW**
   A brief introduction to the importance of viscous fingering as an archetype for growing patterns is given. The main features of non-linearity, non-locality and mixing are explained. Afterwards there is a brief digression about the techniques

1 See respectively Cottet and Komoutsakos [7] and Zabusky, Hughes, and Roberts [33]
2 See respectively Hirt and Nichols [12] and Sethian [25]

used to enable the recovery of oil and the related importance of viscous fingering phenomena. The physical model of the Hele-Shaw flow is analysed and a linear stability analysis, fundamental to understand the mechanism of growth that govern this flow, is presented.

3. **MATHEMATICAL FORMULATION** The governing equations of the Hele-Shaw flow are obtained starting from the incompressible Navier-Stokes equations for multiphase flows. An adimensional formulation of these equations is also obtained and the effect of the governing adimensional parameters is analysed.

4. **NUMERICAL METHOD** The numerical method is described, with particular attention to the treatement of the surface tension and to the interface reconstruction procedure with relation to the topology changes. Peskin's distribution function for the transfer of information between the interface and the fixed grid is introducted.

5. **NUMERICAL EXPERIMENTS** Numerically computed linearized growth rates are presented and compared to analytical results as a first check of the numerical implementation. A number of results of radial fingering simulations are presented in both the cases of static and unsteady pumping.

6. **CONCLUSIONS**

7. **APPENDICES**

2 OIL RECOVERY, VISCOUS FINGERING AND THE HELE-SHAW FLOW

CONTENTS

In a wide variety of situations, formation of patterns results from a growth process. One of these processes is the viscous fingering. This phenomenon has been investigated for fundamental reasons but also because of the needs of industrial research. For instance the petroleum industry has been consistently trying to find ways of inhibiting viscous fingering because it limits oil recovery in a porous media.
During the last thirty years the investigation of a hydrodynamic instability discovered by Saffman and Taylor in 1958 has served as a reference in the field of pattern formation because it has the advantage of being experimentally simple.
Saffman-Taylor fingering is thus studied for reasons beyond its pure hydrodynamic interest, and will be the guiding theme of this chapter.

2.1 INTRODUCTION

Over the past few decades, the interest in numerical modeling of fluid displacement processes has been rising rapidly. The emergence of complex enhanced recovery procedures in the field of hydrocarbon extraction techniques has emphasized the need for mathematical tools capable of modeling sharply changing fluid interfaces, usually unstable.
For an unstable situation small changes in the initial state may amplify rapidly to produce completely different details in interfacial structure at later times. For brevity we shall refer to such behaviour as 'chaotic'. Indeed only certain average properties of an interface may be reproducible in an experiment.
Again, an interface between two fluids, along which there is essentially

no diffusion, may evolve in such a way that substantial entrainment and mixing occur. Both these possibilities are common in conventional turbulent flows, and lead to an efficient macroscopic (as opposed to molecular) mixing.

The equations describing interfaces are generally nonlinear. Analytical investigations of the governing nonlinear equations are usually limited to stability considerations for very regular configurations, such as flat or circular interfaces, and in the limit of small-amplitude disturbances.

The Hele-Shaw cell as a physical model for Saffman-Taylor instability

A relatively simple example of the above type, which however still contains many ingredients of more complicated systems, is the interface between two immiscible fluids in a Hele-Shaw cell , the celebrated Saffman-Taylor instability (Saffman and Taylor [24]), which occurs when a less viscous fluid is forced to penetrate into a more viscous one. This system is two-dimensional by construction, and it is therefore more accessible to numerical calculations.

The initial motivation in the 1950s to study this instability came from the analogy between Hele-Shaw flow and flow in a two-dimensional slab of porous medium.

It was observed that if water was used to drive out residual oil from the porous rock in an oilfield, a considerable amount of oil was left in the ground when water appeared at the producing wells. This disappointing result is believed to be in part due to a fingering instability of the oil-water interface.

Viscous fingering is investigated for fundamental reasons and also for industrial research

Because of its great economic importance , oil-water flow in porous media has been the subject of intensive study in the petroleum-engeneering literature. These studies have been primarily experimental, and their main purpose has been to develop engineering correlations for application to a real field situation.

The discussion of interfaces in a Hele-Shaw cell is commonly divided into the two cases of miscible and immiscible fluids. For immiscible fluids there is a finite surface tension that stabilizes small-scale disturbances. For miscible fluids the interdiffusion of the fluids has a stabilizing effect. If the velocity of interfacial fingers is much higher than the characteristic diffusion velocity, diffusion will not affect the initial shape of the fingers, and they should be similar to those of the immiscible case. Here we consider only immiscible fluids (since that is the case we are capable of calculating numerically), but for the reason just mentioned we believe that some of our conclusions are valid for miscible fluids as well.

Although the applicability of results for fingering in a Hele-Shaw cell to flow under actual reservoir conditions, where the flow is three-dimensional, is not unquestionable, it is to be expected that an investigation of this problem will be helpful to the understanding of many

general properties of unsteady interface motion.

2.2 OIL RECOVERY

Crude oil is found trapped inside the pore-space of rock formations sevaral kilometres below ground. Various techniques have been developed to enable the recovery of oil to the surface, which we now outline. Viscous fingering is important in both secondary and tertiary (enhanced) oil recovery.

2.2.1 Primary and secondary oil recovery

The simplest form of oil recovery is primary oil recovery, in which a well is drilled into the oil reservoir and the oil is pushed up the well due to the naturally high pressure in the oil reservoir. The high pressure is the result of denser rock and water resting above the level of the lighter oil; pockets of trapped compressed gas may also contribute to the higher pressure.

As oil is produced from the well, the natural reservoir pressure drops and the flow of oil to the surface may become greatly reduced. Some techniques that are used to maximise the amount of oil recovered during this primary phase include the use of pumps to lift oil up the well, and the use of explosives and high pressure pumps to fracture the rock formation.

In a typical oil reservoir only around 10 % of the total amount of oil available can be recovered by primary oil recovery. In many oil reservoirs, once primary oil recovery has ceased, more of the oil may still be recovered by secondary oil recovery.

In secondary oil recovery , water is injected into the oil reservoir through one well, displacing the oil so that it can be extracted from a neighbouring well. Since the water is less viscous than the oil and the permeability of the rock is often highly heterogeneous, the time before 'breakthrough', i.e. when the water finds a path between the injection well and the production well, is often very short.

The front is unstable and fingers of water rapidly reach the extraction well and short circuit the motion of the oil

When a large fraction of water is being extracted from the production well, the secondary recovery process becomes uneconomical.

The amount of oil that may thus be extracted depends heavily on the structure of the rock in which the oil is contained and the properties of the oil to be extracted; however, even under optimal conditions more than half of the total amount of oil available will usually be left behind after primary and secondary recovery is complete.

2.2.2 Enhanced oil recovery

With large amounts of oil remaining unrecovered in mature oil reservoirs, the oil recovery industry has developed numerous techniques to extract this oil, referred to under the catchall phrase 'enhanced oil recovery'.

Several techniques are used to reduce the viscosity ratio and consequently the fingering

For some applications thermal recovery is appropriate; here the oil is heated either by the injection of steam or by 'in-situ combustion', where a controlled combustion is started underground using the oil itself as a fuel source. Heating the oil reduces its viscosity thus aiding recovery. Thermal recovery is particularly suited to the extraction of extremely viscous heavy oils, for which the amount recovered by primary and secondary oil recovery is particularly small. When the temperature of heavy oil is increased, its viscosity dramatically decreases, vastly improving the effectiveness of primary and secondary oil recovery techniques.

During secondary recovery, it is possible to add various chemicals to the injected water. The chemicals added are chosen to either increase the viscosity of the water or to be surface active and modify the surface tension at the interface between oil and water.

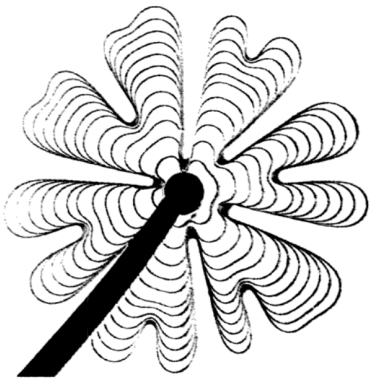

Figure 4: A superposition of successive states of a radial fingering pattern

2.3 VISCOUS FINGERING

The best way to find out what viscous fingering looks like is to do an experiment.

The Hele-Shaw experimental apparatus

Take two circular glass plates , one of them having a central injection hole. Set the plates horizontally, clamped together but separated by thin spacers. First fill the cell with a viscous fluid, e.g. silicon oil, then blow air into the central hole so as to push the oil out radially. An example of what you see in given in figure 4.

Viscous fingering as am archetype for growth patterns in a Laplacian field

The air does not penetrate the oil regularly to form a circular region but forms a pattern which becomes increasingly complex. In this instability, the two fluids and their interface move due to the applied pressure. The two fluids have a Poiseuille flow driven by the applied pressure. The experimental situation can thus be described by a two-dimensional model where the spatial distribution of pressure forms a Laplacian field and the fluids move with a velocity proportional to the gradient of pressure (Couder [8]).
An interface separates two regions of a plane respectively labelled (1) and (2). There exist a scalar field $P(x, y, z)$ in this plane; in our case this field P is the pressure. In the simplest case P is constant in region 1 and in region 2 satisfies the Laplacian:

$$\nabla^2 P = 0 \tag{2.1}$$

At a given time, the determination of the field P depends on the boundary conditions defined at infinity and at the interface between regions 1 and 2. We are interested in situations in which this interface moves in the local gradient of P with a normal velocity

$$V_n \propto \hat{\mathbf{n}} \cdot \nabla P \tag{2.2}$$

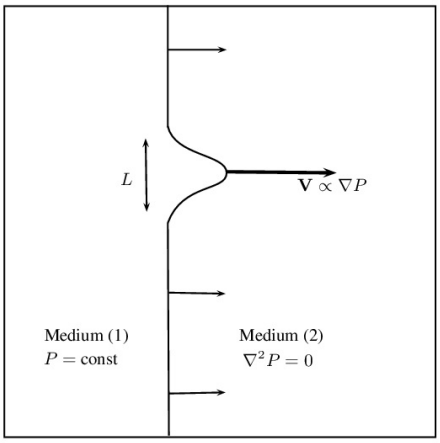

Figure 5: Saffman-Taylor instability

where $\hat{\mathbf{n}}$ is the unit vector normal to the interface. The displacement of the interface, because it changes the location of a boundary, modifies the field P and thus, in turn, the interface velocity. This process leads to an instability, the Saffman-Taylor instability, which generates a pattern. The whole process is strongly non-local , due to the long-range interactions introduced by Laplace's law.

Non-locality

We consider a situation where the two fluids are initially separated by a flat interface and we assume this interface to be disturbed by a small protrusion of typical size L (figure 5). The curves at constant values of P will be parallel lines, only distorted in front of the bump. It is a property of Laplacian fields that the distortion will only affect these curves to a 'depth' of order of L. As a result the gradient of P is locally larger in front of the protrusion and so is the velocity. The amplitude of the protrusion will thus grow: the interface is unstable.

Note that if the fluids were moving in the opposite direction, i.e. if the more viscous fluid was forcing the less-viscous one to retrocede, the change in velocity would serve to reduce the protrusion and the front would be stable.

Ideally, in the absence of any other factor, the more pointed the protrusion the larger the gradient and the velocity. In real experiments, additional effects due to the interfacial capillarity effect are present which stabilize the interface at small scales.

2.4 THE HELE-SHAW FLOW

Henry Selby Hele-Shaw (1854-1941) was an English mechanical and automobile engineer

Hele-Shaw flow (named after Henry Selby Hele-Shaw) is defined ad Stokes flow between two parallel flat plates separated by an infinitesimally small gap (figure 6).

The Hele-Shaw problem is a prototypical free-boundary problem that shares many of the difficulties often encountered in simulations of dynamic boundaries in fluids: the incompressibility condition leads to an elliptic (Laplace) equation for pressure that must be solved in the time-dependent domain created by the free boundary dynamics; in the approach followed by many authors (Fast and Shelley [10]) the computational domain consists of the space occupied by the external fluid, with boundary conditions imposed at the interface and at the outflow. This approach is valid in the case in which the internal fluid has a negligible viscosity with respect to the external one: this can be explained looking at the governig equations. Since the inertial terms are negligibly smaller than the pressure or the viscous terms, in the limit of zero Re, we have the basics equation of Stokes flow:

$$0 = -\nabla p + \mu \nabla^2 \mathbf{u} \tag{2.3}$$

Considering a negligible viscosity for the internal flow we obtain that $\nabla p = 0$ and thus the pressure is constant. Moreover, from continuity we have:

$$\nabla \cdot \mathbf{u} = 0 \tag{2.4}$$

Since the thickness is small, only the velocity components parallel to the plates are considered. Their dominant variation is in the z-direction so that 2.3 can be written

$$\nabla p = \mu \frac{\partial^2 \mathbf{u}}{\partial z^2} \tag{2.5}$$

which can be integrated to give the parabolic velocity field of plane Poiseuille flow :

The flow in a Hele-Shaw cell is a locally plane Poiseuille flow

$$\mathbf{u} = \frac{1}{2\mu} z(z-b)\nabla p \tag{2.6}$$

Integrating the flow through the cell thickness, we define an average velocity $\langle \mathbf{u} \rangle$ by

$$\int_0^b \mathbf{u} dz = \langle \mathbf{u} \rangle b \tag{2.7}$$

and find that $\langle \mathbf{u} \rangle$ is governed by the potential law

$$\langle \mathbf{u} \rangle = -\frac{b^2}{12\mu} \nabla p. \tag{2.8}$$

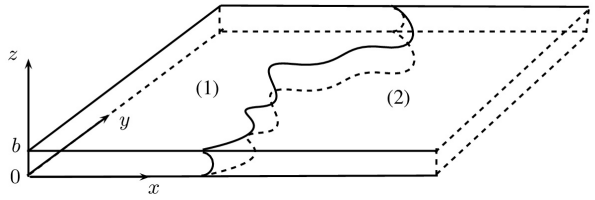

Figure 6: Sketch of the Hele-Shaw cell

This relation between mean velocity and pressure is a particular case of Darcy's law, which holds more generally for fluids moving through porous media such e.g. rocks. It is usually written

$$\langle \mathbf{u} \rangle = -\frac{K}{\mu} \nabla p \tag{2.9}$$

Darcy's law was formulated by Henry Darcy based on the results of experiments on the flow of water through beds of sand

where K is the permeability of the medium.
Finally, in both a Hele-Shaw cell and in a porous medium, since the fluid is incompressible, $\nabla \cdot \langle \mathbf{u} \rangle = 0$ and the pressure is a Laplacian field,

$$\nabla^2 p = 0 \tag{2.10}$$

In the following we will adopt the two-dimensional approximation where the velocities of the fluid are the average ones satisfying relation 2.8, and we will omit the average symbol.

If we don't want to neglect the viscosity of the internal fluid, we can observe that equation 2.8 is valid also for the less viscoud fluid, so that we can write:

$$\mathbf{u}_j = -\frac{b^2}{12\mu_j} \nabla p_j \qquad j = 1, 2 \tag{2.11}$$

where the subscripts 1 and 2 are used to refer to the inner and outer fluid respectively. In this case we have to add a source term in the continuity equation for the internal domain to take into account the injection of fluid into the cell:

$$\nabla \mathbf{u}_1 = Q\delta(\mathbf{x} - \mathbf{x}_s) \tag{2.12}$$

2.4.1 Boundary conditions

The boundary conditions must be specified at the interface between the two fluids and at the outer edge of the cell. The jump conditions across the interface is

$$[p]_\Gamma = \sigma\kappa = \sigma\left(\frac{2}{b} + \kappa_{2d}\right) \tag{2.13}$$

where σ is the surface tension and κ is the curvature of the interface, composed by two terms: the curvature of the meniscus and that in the $x-y$ plane; the kinematic condition is

The dimension of the surface tension is [Force]/[Length]

$$\frac{\partial \mathbf{u}}{\partial t}(\beta, t) = \mathbf{u}|_{\mathbf{x}(\beta,t)}, \tag{2.14}$$

where β is a Lagrangian parameter.
We consider for simplicity the flow in a circular Hele-Shaw cell with radius R_{out}. To determine the outflow boundary condition we assume that the interface is far away from the outflow boundary, so that the flow at the boundary agrees with the radial outflow, which would arise from the source term in a uniform fluid; thus at the outer edge of the cell ($r = R_{out}$), we impose a specified mass flux Q through the outflow condition

$$\hat{\mathbf{r}} \cdot \mathbf{u} = \frac{Q}{2\pi R_{out}} \tag{2.15}$$

where $\hat{\mathbf{r}}$ is a unit vector in the radial direction. In terms of the pressure, the outflow boundary condition at $r = R_{out}$ is

$$\frac{\partial p}{\partial r} = -\frac{12\mu_2}{b^2}\frac{Q}{2\pi R_{out}}. \tag{2.16}$$

that can be integrated in order to obtain the following Dirichlet boundary condition:

$$p(R_{out}) = p_0 - \frac{12\mu_2}{b^2}\frac{Q}{2\pi} log(R_{out}) \tag{2.17}$$

where p_0 is some arbitrary constant. This leads to the bubble area growing at a specified rate.

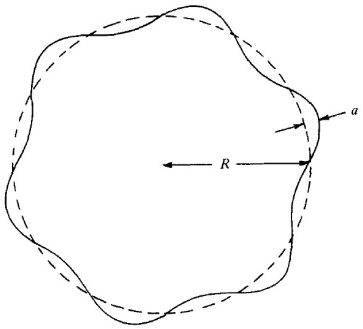

Figure 7: A circular interface of radius R with a wavelike perturbation a

2.5 A LINEAR STABILITY ANALYSIS

Chuoke, van Meurs, and van der Pol [6] have made studies of the initial growth of fingers from a linear interface. In particular they have shown that surface tension prevents fingers from occurring below a certein wavelenght, where wavelength is defined as peak-to-peak separation. The problem of the instability of an initially circular interface has been examined elsewhere (Bataille [3]).
Equation 2.11 in polar coordinates leads to

$$\frac{\partial^2 \phi_j}{\partial r^2} + \frac{1}{r}\frac{\partial \phi_j}{\partial r} + \frac{1}{r^2}\frac{\partial^2 \phi_j}{\partial \theta^2} = 0 \qquad j = 1, 2 \tag{2.18}$$

where $\phi_j = b^2/(12\mu_j)p_j$ is the velocity potential.
The source has volume flow rate Qb and the circle has radius R, so that, for unperturbed displacements,

$$R(t) = \sqrt{(Qt + \pi R_0^2)/\pi} \tag{2.19}$$

The velocity potential of the steady flow can be derived from 2.18 as

$$\phi_j^{(0)} = -\frac{Q}{2\pi}\left(ln\frac{r}{R} + \frac{\mu_2}{\mu_j}\right). \tag{2.20}$$

Equation 2.20 satisfies the continuity of pressure and radial velocity at the interface $r = R(t)$.
As the interface moves, it experiences perturbations due to inhomogenities. Any perturbation can be expressed as an infinite sum of wavelike functions. For the purpose of the following linear analysis, it is sufficient to consider a single wavelike perturbation a with amplitude A, as shown in figure 7, so that

$$a(n,t,\theta) = Af(n,t)e^{in\theta} \qquad n = 1,2,3... \tag{2.21}$$

where $f(n,t)$ represent the dependence of the amplitude on time. The required solution of 2.18, with β to be determined, is

$$\phi_j = \phi_j^{(0)} + (-1)^j \beta \left(\frac{r^n}{R^n}\right)^{(-1)^{j-1}} e^{in\theta}. \tag{2.22}$$

The condition of continuity at the perturbed interface (to first order at $r = R(t)$) determines β as

$$\beta = \frac{A}{n}\left(\frac{Qf}{2\pi R} R \frac{df}{dt}\right). \tag{2.23}$$

The pressure drop across the interface depends on the surface tension σ through

$$p_1 - p_2 = \sigma\left(\frac{2}{b} + \frac{1}{R} - \frac{a + d^2a/d\theta^2}{R^2}\right) \tag{2.24}$$

to first order, since $r = R + a$. Using the equations from 2.20 to 2.24 gives

$$\frac{df}{dt} = \frac{Qn}{2\pi R^2}\left(\frac{K_1 - K_2}{K_1 + K_2}\right) - \frac{Q}{2\pi R^2} - \frac{\sigma n(n^2-1)}{R^3}\left(\frac{K_1 K_2}{K_1 + K_2}\right) f \tag{2.25}$$

The term

$$\frac{Qn}{2\pi R^2}\left(\frac{K_1 - K_2}{K_1 + K_2}\right) - \frac{Q}{2\pi R^2} - \frac{\sigma n(n^2-1)}{R^3}\left(\frac{K_1 K_2}{K_1 + K_2}\right) \tag{2.26}$$

is the *growth rate* of the perturbations. If $K_1 \gg K_2$[1] it becomes:

The symbol σ_n for the growth rate is used for agreement with the literature and must not be confused with the surface tension σ

$$\sigma_n = \frac{n-1}{R^2}\left(\frac{Q}{2\pi} - \frac{n(n+1)\sigma K_2}{R}\right) \tag{2.27}$$

The condition $df/dt = 0$ gives rise to a minimum wavelength λ_c, for a perturbation to be mantained. With this condition, equation 2.25 can be solved for n to give

$$n_c = \sqrt{\frac{QR}{2\pi K_2 \sigma} + \frac{1}{4}} - \frac{1}{2}. \tag{2.28}$$

1 For a constant injection rate, we obtain a Mullins-Sekerka type instability; it is involved in the study of the morphological instability of a solid-liquid interface during solidification. In this situation the classical thermodynamic definition of stability is no longer applicable in determining the morphology of the growing interface.

Since $n = 2\pi R/\lambda$, this gives the critical wavelength λ_c as

$$\lambda_c = 2\pi R \Big/ \left(\sqrt{\frac{QR}{2\pi K_2 \sigma} + \frac{1}{4}} - \frac{1}{2} \right) \tag{2.29}$$

Maximum growth occurs when

$$\frac{\partial}{\partial n} \left(\frac{df}{dt} \right) = 0 \tag{2.30}$$

whic, from 2.25, leads

$$n_m = \sqrt{\frac{1}{3} \left(\frac{QR}{2\pi K_2 \sigma} + 1 \right)}, \tag{2.31}$$

or substituting $n = 2\pi R/\lambda$ leads to a wavelength of maximum growth rate, λ_m:

$$\lambda_m = 2\sqrt{3}\pi R \Big/ \sqrt{\frac{QR}{2\pi K_2 + 1} + 1} \tag{2.32}$$

The key feature is that the intermediate length-scales are unstable and the small length-scales are strongly damped

Equation 2.25 shows the competition between the destabilizing effect due to injection and the stabilizing effect due to the surface tension. Note that, for high frequency modes, σ_n is negative, indicating that the Hele-Shaw flow is stable for these frequencies. For lower frequencies, depending on the parameters, σ_n can be positive, indicating unstable growth. For a zero surface tension σ_n scales with n, and the system is linearly ill-posed (the growth rates are unbounded for $k \to \infty$ [2]. The case with $n = 0$ leads to a zero growth rate, which can be explained with the fact that it involves only a translation of the initial circular interface. Paterson [21] investigated these aspects with an experiment; in his example $Q = 9.3$ cm$^2/s$, $b = 0.15$ cm and $\sigma = 63$ dyne/cm. The temperature was 28°C at which $K_2 = 3.6 \cdot 10^{-4}$ (cm^4/dyne)/s. He showed that the fingers appear to have wavelength λ_m at their inception.

In figure 8 we can see the typical trend of the growth-rate as a function of the wavenumber of the azimutal perturbation for a given value of R.

In figure 9 the initial radius dependence of the critical wave length and of the wave length of maximum growth rate is reported.

2 This is very similar to the linearized behaviour associated with the Kelvin-Helmotz instability of Eulerian fluid dynamics

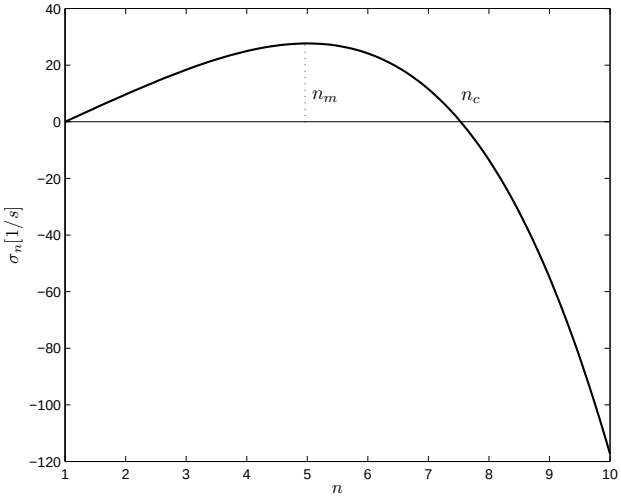

Figure 8: The wave number dependence of the amplification rate predicted by the linear analysis of viscous fingering. The parameters are those of Paterson's experiment.

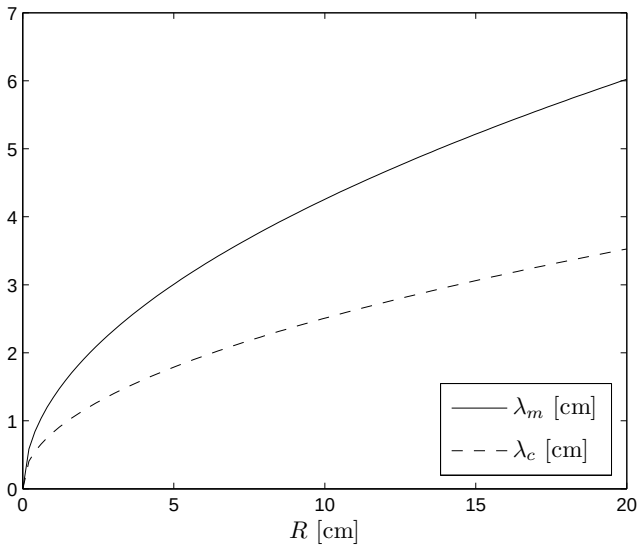

Figure 9: The initial radius dependence of the critical wave length and of the wave length of maximum growth rate. The parameters are those of Paterson's experiment.

3 MATHEMATICAL FORMULATION

CONTENTS

In this chapter an innovative mathematical formulation for the problem under investigation is presented. The method is based on writing one set of governing equations for the whole computational domain and treating the different phases as one fluid with variable material properties. Interfacial terms are accounted for by adding the appropriate sources as $\delta-$functions at the boundary separating the phases.

3.1 CONSERVATION EQUATIONS

The key of this method, as well as to several other methods to simulate multiphase flow, is the use of a single set of conservation equations for the whole flow field.
In addition to accounting for differences in the material properties of the different fluids, we must include interfacial phenomena such as surface tension by adding the appropriate interface terms to the governing equations . Since these terms are concentrated at the boundary between the different fluids, they are represented by δ-functions. Since the material properties and the flow field are, in general, discontinuos across the interface all variables must be interpreted in terms of generalized functions. This approach is presented in Tryggvason et al. [30] and Shin and Juric [26].

Interfacial terms are accounted for as δ-functions

Before we write down the equations governing multiphase flow it is useful to discuss a few elementary aspects of the representation of a discontinuous function by generalized functions. The various fluids can be identified by a step (Heaviside) function H which is 1 where one particular fluid is and 0 elsewhere; we call this step function the *indicator function*. The interface itself is marked by a non-zero value of the gradient of the step function. To relate the gradient to the δ-

function marking the interface, it is most convenient to express H in terms of an integral over the product of one-dimentional δ-functions:

$$H(\mathbf{x},t) = \int_{A(t)} \delta(\mathbf{x}-\mathbf{x}')da' \tag{3.1}$$

The integral is over an area $A(t)$ boundend by a contour $\Gamma(t)$. I is obviously 1 if $\mathbf{x}$ is enclosed by Γ and 0 otherwise. To find the gradient of H we note first that since the gradient is with respect to the unprimed variables, the gradient operator can be put under the integral sign. Since the δ-functions are anti-symmetric with respect to the primed and unprimed variables, the gradient with respect to the unprimed variables can be replaced by the the gradient with respect to the primed variables. The resulting area integral can be transformed into a line integral by a variation of the divergence theorem for gradients. Symobolically:

$$\begin{aligned}\nabla H = \int_{A(t)} \nabla\delta(\mathbf{x}-\mathbf{x}')da' &= -\int_{A(t)} \nabla'\delta(\mathbf{x}-\mathbf{x}')da' \\ &= -\oint_{\Gamma(t)} \delta(\mathbf{x}-\mathbf{x}_f)\hat{\mathbf{n}}ds\end{aligned} \tag{3.2}$$

where $\hat{\mathbf{n}}$ is the outward unit normal to the interface and $\mathbf{x}_f = \mathbf{x}(s,t)$ is a parametrization of the interface $\Gamma(t)$. By considering an inward unit normal and applying the divergence to equation 3.14 we obtain the governing Poisson equation for the indicator function $H(\mathbf{x},t)$:

$$\nabla^2 H = \nabla \cdot \int_{\Gamma(t)} \hat{\mathbf{n}}\delta(\mathbf{x}-\mathbf{x}_f)ds \tag{3.3}$$

The values of the material property fields at every location can then be given by

$$b(\mathbf{x},t) = b_2 + (b_1 - b_2)H(\mathbf{x},t) \tag{3.4}$$

where subscript 1 and 2 refers respectively to the inner and outer fluid and b stands for density ρ or viscosity μ. For example the gradient of the viscosity is given by:

$$\nabla\mu = (\mu_1-\mu_2)\nabla H(\mathbf{x},t) = (\mu_1-\mu_2)\int_{\Gamma(t)} \delta(\mathbf{x}-\mathbf{x}_f)\hat{\mathbf{n}}ds \tag{3.5}$$

Note that the right-hand side of this Poisson equation is a function only of the known interface position, a fact we use to advantage in our

numerical implementation.
The interface is advected in a Lagrangian fashion by integrating

$$\frac{d\mathbf{x}_f}{dt} = \mathbf{u}_f \tag{3.6}$$

where $\mathbf{u}_f = \mathbf{u}(\mathbf{x}_f)$ is the fluid velocity at the interface. Only the normal component of the interface motion is determined by the physics. The tangential motion is not and we may assume that the interface and fluid at the interface have the same tangential component of velocity (Shin and Juric [26]).

Mass conservation is given by

$$\frac{\partial \rho}{\partial t} + \nabla \cdot \rho \mathbf{u} = 0 \tag{3.7}$$

The fluids are taken to be incompressible so that the density of a fluid particle remains constant:

$$\frac{D\rho}{Dt} = 0 \tag{3.8}$$

This reduces the mass conservation to

$$\nabla \cdot \mathbf{u} = 0; \tag{3.9}$$

we want also a source/sink of mass in the domain to pump/suck fluid into/from the cell. Hence, the equation of continuity becomes: *Continuity equation*

$$\nabla \cdot \mathbf{u} = Q(t)\delta(\mathbf{x} - \mathbf{x}_s). \tag{3.10}$$

We also take the viscosity in each fluid to be constant:

$$\frac{D\mu}{Dt} = 0 \tag{3.11}$$

The momentum equation is written for the entire flow field and the forces due to surface tension are inserted at the interface as body forces, which act only at the interface. In conservative form this equation, neglecting the inertial and non stationary terms, is *Momentum equation*

$$0 = -\nabla p + \nabla \cdot \mu(\nabla \mathbf{u} + \nabla \mathbf{u}^T) + \int_{\Gamma(t)} \sigma \kappa \hat{\mathbf{n}} \delta(\mathbf{x} - \mathbf{x}_f) ds \tag{3.12}$$

The integral term in 3.12 accounts for surface tension acting on the interface. (Following the discussion of Tryggvason et al. [30] we ignore

tangential variations in σ along the interface).
Introducing the same hypothesis introduced in section 2.4 we obtain

$$0 = -\nabla p + \mu \frac{\partial^2 \mathbf{u}}{\partial z^2} + \int_{\Gamma(t)} \sigma \kappa \hat{\mathbf{n}} \delta(\mathbf{x} - \mathbf{x}_f) ds \tag{3.13}$$

where now $\mathbf{u} = (u, v)$. Integrating over the gap and averaging we have

$$< \mathbf{u} >= -\frac{b^2}{12\mu} \left(\nabla p - \int_{\Gamma(t)} \sigma \kappa \hat{\mathbf{n}} \delta(\mathbf{x} - \mathbf{x}_f) ds \right). \tag{3.14}$$

where now the integral is a line integral over the interface. Two dimensionality has been enforced by neglecting three dimensional effects but the consequent loss of realism is usually considered unimportant; a global effect of the tridimensionality can be included by adding the curvature meniscus $2/b$ at the bidimensional curvature, as was done in equation 2.13.

Applying the divergence to equation 3.14 and using equation 3.10 we obtain this elliptic equation for the pressure:

$$\nabla \cdot \left(-\frac{b^2}{12\mu} \nabla p \right) = Q(t) \delta(\mathbf{x} - \mathbf{x}_s) - \nabla \cdot \left(\frac{b^2}{12\mu} \int_{\Gamma(t)} \sigma \kappa \hat{\mathbf{n}} \delta(\mathbf{x} - \mathbf{x}_f) ds \right). \tag{3.15}$$

The boundary conditions must be specified only at the outflow; in particular the condition 2.17 must be applied at the external boundary of the domain.
Defining $\beta = -b^2/(12\mu)$ we can write the following system of equations

The $\delta-$ functions have the dimension of $1/[length^2]$

GOVERNING EQUATIONS

$$\begin{cases} \nabla \cdot (\beta \nabla p) = Q(t) \delta(\mathbf{x} - \mathbf{x}_s) + \nabla \cdot \left(\beta \int_{\Gamma(t)} \sigma \kappa \hat{\mathbf{n}} \delta(\mathbf{x} - \mathbf{x}_f) ds \right), \\ \mathbf{u} = \beta \left(\nabla p - \int_{\Gamma(t)} \sigma \kappa \hat{\mathbf{n}} \delta(\mathbf{x} - \mathbf{x}_f) ds \right). \end{cases} \tag{3.16}$$

BOUNDARY CONDITIONS

$$p(R_{out}) = p_0 + \frac{1}{\beta_{out}} \frac{Q}{2\pi} log(R_{out})$$

This system can be solved by solving the first equation for the pressure separately and then recovering the velocity field from the second equation.
Since, being a constant term, it doesn't affect the velocity field (and thus the development of the fingers) we will neglet the surface tension term depending on the meniscus curvature.

3.2 ADIMENSIONAL FORM

In this section the adimensional form of the equations 3.22 will be derived, in order to obtain the adimensional parameters governing the physic of the problem.
Let us introduce the following reference values for the different physical quantities:

$$L_R = b; \qquad \mu_R = \mu_2;$$

$$p_R = \sigma/b; \quad U_R = Q/b.$$

This allows us to write the following dimensionless variables:

$$\mathbf{x}^* = \frac{\mathbf{x}}{L_R} = \frac{\mathbf{x}}{b}; \qquad \mathbf{u}^* = \frac{\mathbf{u}}{U_R} = \frac{\mathbf{u}}{Q/b};$$

$$p^* = \frac{p}{p_R} = \frac{p}{\sigma/b}; \qquad \mu^* = \frac{\mu}{\mu_R} = \frac{\mu}{\mu_2};$$

$$\delta^* = \frac{\delta}{1/L_R^2} = \frac{\delta}{1/b^2}; \quad \kappa^* = \frac{\kappa}{1/L_R} = \frac{\kappa}{1/b}.$$

Substituting into the mass conservation equation we obtain the following adimensional equation:

$$\nabla^* \cdot \mathbf{u}^* = \delta^*(\mathbf{x}^* - \mathbf{x}_s^*) \tag{3.17}$$

With the same substitutions quation 3.14 becomes:

$$\mathbf{u}^* = -\frac{\sigma b}{12\mu_2 Q}\frac{1}{\mu^*}\left(\nabla^* p^* - \int \kappa^* \hat{\mathbf{n}} \delta^*(\mathbf{x}^* - \mathbf{x}_f^*) ds^*\right) \tag{3.18}$$

Applying a 'nondimensional' divergence to equation 3.18 we obtain the following elliptic equation for the adimensional pressure:

$$\begin{aligned}\nabla^* \cdot \left(-\frac{1}{\mu^*}\nabla^* p^*\right) =& \frac{12\mu_2 Q}{\sigma b}\delta^*(\mathbf{x}^* - \mathbf{x}_s^*) \\ &+ \nabla^* \cdot \left(-\frac{1}{\mu^*}\int \kappa^* \hat{\mathbf{n}}\delta^*(\mathbf{x}^* - \mathbf{x}_f^*)ds^*\right)\end{aligned} \tag{3.19}$$

The nondimensional form of the Dirichlet boundary condition is the following:

$$p^*(R_{out}^*) = -\frac{12\mu_2 Q}{\sigma b}\frac{1}{2\pi}log(r^*) \tag{3.20}$$

Concluding we discovered that two adimensional parameters determine the physics of the problem; these two parameters are the following[1]:

VISCOSITY RATIO

$$\frac{\mu_1}{\mu_2}$$

SURFACE TENSION PARAMETER

$$A = \frac{12\mu_2 Q}{\sigma b}$$

The viscosity ratio parameters enters in the definition of the variable μ^*, which has the following expression:

$$\mu^* = 1 + \left(\frac{\mu_1}{\mu_2} - 1\right) H(\mathbf{x}, t) \tag{3.21}$$

and thus assumes the value 1 outside of the interface and μ_1/μ_2 within it.
Substituting these definitions we obtain the following system of nondimentional equations:

NONDIMENSIONAL GOVERNING EQUATIONS

$$\begin{cases} \nabla^* \cdot \left(-\frac{1}{\mu^*}\nabla^* p^*\right) = A\delta^*(\mathbf{x}^* - \mathbf{x}_s^*) \\ \qquad\qquad + \nabla^* \cdot \left(-\frac{1}{\mu^*}\int \kappa^* \hat{\mathbf{n}}\delta^*(\mathbf{x}^* - \mathbf{x}_f^*)ds^*\right) \\ \mathbf{u}^* = -\frac{1}{A}\frac{1}{\mu^*}\left(\nabla^* p^* - \int \kappa^* \hat{\mathbf{n}}\delta^*(\mathbf{x}^* - \mathbf{x}_f^*)ds^*\right) \end{cases} \tag{3.22}$$

1 Unfortunately no universal convenction for this controlling parameters has been adopted in the literature, and care must be taken in comparing results of different investigators

NONDIMENSIONAL BOUNDARY CONDITIONS

$$p^*(R^*_{out}) = -A\frac{1}{2\pi}log(r^*)$$

3.2.1 The nondimensional growth rate equation

Now we can proceed by adimensionalising the equation for the growth rate of the perturbation in the linear analysis (2.25).
The following reference time is introduced:

$$T_R = \frac{L_R^2}{Q} = \frac{b^2}{Q}$$

so that the nondimensional growth rate σ_n^* can be defined:

$$\sigma_n^* = \frac{\sigma_n}{T_R} = \frac{\sigma_n}{b^2/Q}$$

The nondimensional form of equation 2.25 is

$$\sigma_n^* = \frac{n}{2\pi R^{*2}}\frac{(1-\mu_1/\mu_2)}{(1+\mu_1/\mu_2)} - \frac{1}{2\pi R^{*2}} - \frac{1}{A}\frac{n(n^2-1)}{R^{*3}(1+\mu_1/\mu_2)} \tag{3.23}$$

which in the limit $\mu_1/\mu_2 \to 0$ becomes:

$$\sigma_n^* = \frac{n-1}{2\pi R^{*2}} - \frac{1}{A}\frac{n(n^2-1)}{R^{*3}} \tag{3.24}$$

Effect of the parameters

The nondimensional growth rate from equation 3.23 is influenced by three parameters: the initial radius R, the surface tension parameter A and the viscosity ratio μ_1/μ_2. The effect of these parameters can be seen in the figures 10, 11 and 12. We observe from figure 10 that if we increase the initial radius of the circular interface, the band of unstable wavenumbers become larger and the intensity of the growth smaller.
The graphic of figure 11 can be explained as follows: an increment of the tension parameter A can be viewed as a reduction of the physical surface tension σ keeping constant the mass flow rate Q or as an increment of Q keeping constant σ. This results in a more emphasized instability in terms of maximum unstable wavelength and values of the growth-rate.

If we increase A we observe a stronger growth process

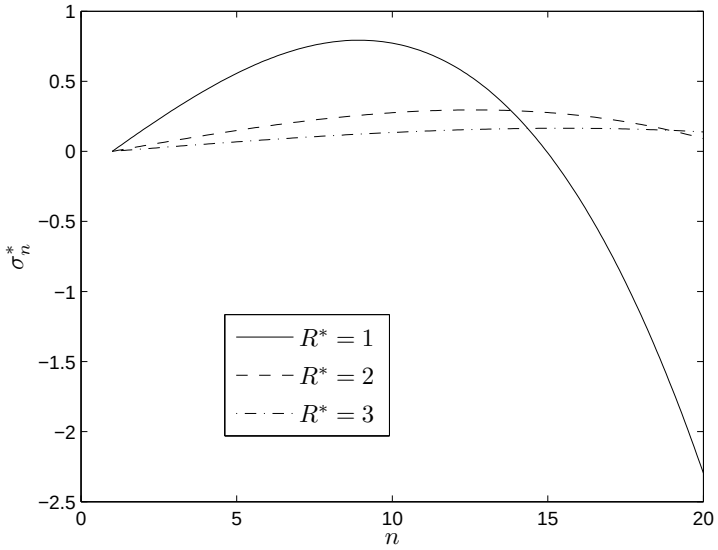

Figure 10: Effect of the initial radius of the interface on the growth rate of the perturbations ($\mu_1/\mu_2 \to 0$, $A = 1.5 \cdot 10^3$)

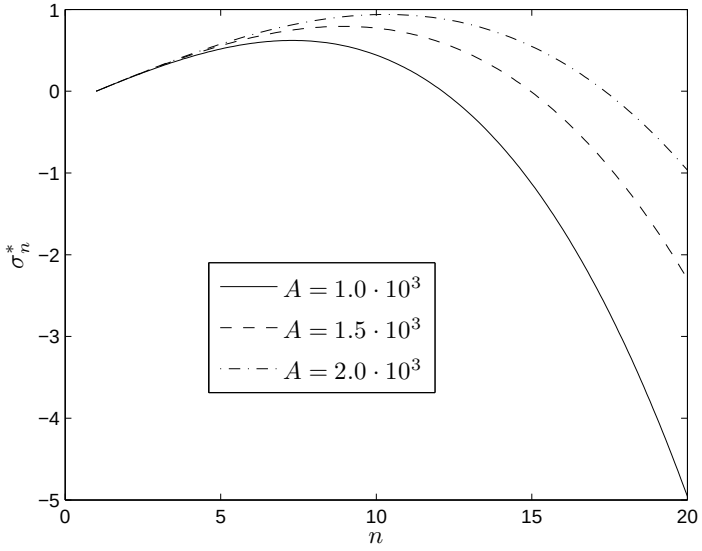

Figure 11: Effect of the surface tension parameter on the growth rate of the perturbations ($\mu_1/\mu_2 \to 0$, $R = 1$)

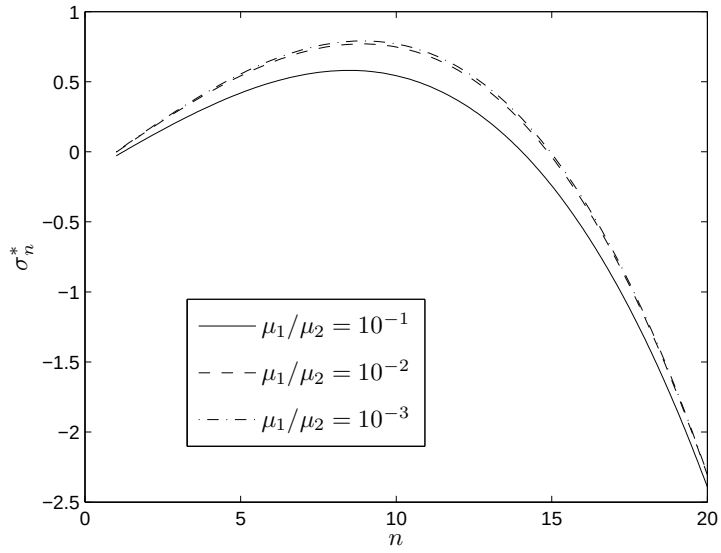

Figure 12: Effect of the viscosity ratio on the growth rate of the perturbations ($R = 1$, $A = 1.5 \cdot 10^3$)

In figure 12 the effect of the viscosity ratio is reported: the width of the unstable band remains the same, but as we can expect the growth rates become bigger decreasing the viscosity ratio. In the limit $\mu_1/\mu_2 \to 0$ we obtain the same behaviour of equation 3.24.

4 NUMERICAL METHOD

CONTENTS

The formulation descrived in chapter 3 allows multiphase flows to be treated along the lines usually used for homogeneous flows. Once the material boundary as been advected and the surface tension found, any standard algorithmn based on fixed grids can, in principle be used to integrate equation 3.22. Figure 13 summarizes the approach: a fixed grid is used for the conservation equations but a moving grid of lower dimension marks the boundary between the different phases. This moving grid is represented by nonstationary, Lagrangian computational points connected to form a line.

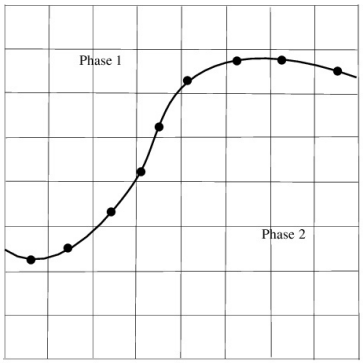

Figure 13: Stationary finite difference mesh and moving Lagrangian mesh

4.1 TRANSFER OF INFORMATION BETWEEN THE INTERFACE AND THE FIXED GRID

At each time step information must be passed between the moving Lagrangian interface and the stationary Eulerian grid. Since the Lagrangian interface points $\mathbf{x}_p$ do not coincide with the Eulerian grid points $\mathbf{x}_{ij}$, this is done using Peskin's immersed boundary method (Peskin [22]). With this technique, the infinitely thin interface is approximated by a smooth distribution function that is used to distribute sources at the interface over several grid points near the interface (since the front represent a $\delta-$function, the transfer corresponds to the construction of an approximation to this $\delta-$function on the fixed grid). In similar manner, this function is used to interpolate field variables (velocities) from the stationary grid to the interface.
In this way the front is given a finite thickness on the order of the mesh size to provide stability and smoothness. There is also no numerical diffusion since the thickness remains constant for all time.
It is always necessary to ensure that the quantity transferred is conserved. The interface quantity, ϕ, is usually expressed in units per length, but the grid value, Φ, should be given in terms of units per area.
To ensure that the total value is conserved in the smoothing, we ust therefore require that:

$$\int_{\Delta s} \phi(s) ds = \int_{\Delta a} \Phi(\mathbf{x}) da \tag{4.1}$$

This is accomplished by writing

$$\Phi_{ij} = \sum_p \phi_p D_{ij}(\mathbf{x}_p) \frac{\Delta s_p}{\Delta x \Delta y} \tag{4.2}$$

Here ϕ_p is a discrete approximation to the front value $\phi(s)$ and Φ_{ij} is an approximation to the grid value $\Phi(\mathbf{x})$. Δs_p is the length of the element p. $D_{ij}(\mathbf{x}_p)$ is the weight of grid point ij with respect to element p. The weights must satisfy:

$$\sum_{ij} D_{ij} = 1 \tag{4.3}$$

Since the weight have a finite support, there is a relatively small number of front elements that contribute to the value at each fixed grid point. In the actual implementation of the transfer of quantities from the front to the grid, we loop over the interface elements and add

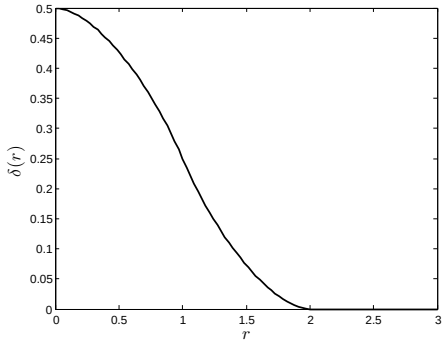

Figure 14: Distribution function

the quantity to the grid points that are near the front.
The weighting functions are usually written as a product of one-dimensional functions:

$$D_{ij}(\mathbf{x}_p) = \delta\left(\frac{x_p - x_i}{\Delta x}\right)\delta\left(\frac{y_p - y_j}{\Delta y}\right) \tag{4.4}$$

We use the distribution function (figure 14) suggested by Peskin and McQueen [23], so that

$$\delta(r) = \begin{cases} \delta_1(r), & |r| \leq 1 \\ 1/2 - \delta_1(2 - |r|), & 1 < |r| < 2 \\ 0, & |r| \geq 2 \end{cases}$$

and

$$\delta_1(r) = \frac{3 - 2|r| + \sqrt{1 + 4|r| - 4r^2}}{8}$$

With the same function we can transfer information from the grid to the interface; at each time step the velocity field is calculated on the fixed grid but we need the velocity of the interface points in order to start the advection routine. The interpolation is achieved with the following expression:

$$\mathbf{u}_p = \sum_{ij} \mathbf{u}_{ij} D_{ij}(\mathbf{x}_p) \tag{4.5}$$

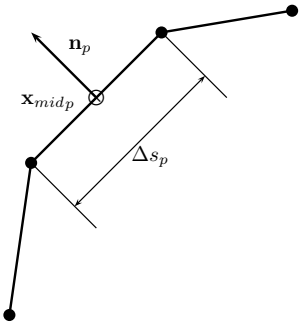

Figure 15: Surface integral calculation for the indicator function. The normal and area provided to the integral are readily defined

4.2 UPDATING THE MATERIAL PROPERTIES

The fluid properties, and particularly the viscosity, are not advected directly. Instead the boundary between the different fluids is moved. It is therefore necessary to reset the properties at every time step.
To do that, we first find the indicator function (we assume that the interface location is known) using a fast Poisson solver for 3.3

$$\nabla_h^2 H = \nabla_h \cdot \mathbf{N}. \tag{4.6}$$

*In the discretized form of the equations the superscript * for nondimensional variables will be omitted*

The subscript h denotes the finite difference approximation to the operator. Here $\mathbf{N}$ is the approximation to the surface integral in 3.3 :

$$\mathbf{N}_{i,j} = \sum_p \hat{\mathbf{n}}_p \frac{D_{ij}(\mathbf{x}_{mid\,p})}{\Delta x \Delta y} \Delta s_p \sim \int \hat{\mathbf{n}} \delta^*(\mathbf{x} - \mathbf{x}_f) ds^* \tag{4.7}$$

Note that the sources are located at the centroid of each element and then distributed by the immersed boundary method as described previously. $\hat{\mathbf{n}}_p$ is computed by considering that the interface element is a segment connecting the two end-points (figure 15).

The indicator function calculated in this way is constant within each material region but has a finite thickness transition zone around the interface. In this transition zone the indicator function and thus the material properties change smoothly from the value on one side of the interface to the value on the other side (figure 16).
The thickness of the transition zone is only a function of the mesh size and is constant during the calculation (no numerical diffusion is introduced).

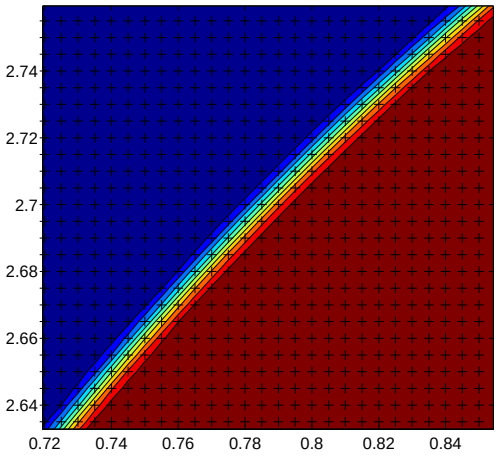

Figure 16: Thickness of the transition zone

The discretized form of equation 3.3 is:

$$\frac{H_{i+1,j} - 2H_{i,j} + H_{i-1,j}}{\Delta x^2} + \frac{H_{i,j+1} - 2H_{i,j} + H_{i,j-1}}{\Delta y^2} = \frac{(N_x)_{i+\frac{1}{2},j} - (N_x)_{i-\frac{1}{2},j}}{\Delta x} + \frac{(N_y)_{i,j+\frac{1}{2}} - (N_y)_{i,j-\frac{1}{2}}}{\Delta y} \tag{4.8}$$

where me make use of the following definitions:

$$x_{i\pm\frac{1}{2}} = \frac{x_i + x_{i\pm\frac{1}{2}}}{2}; \qquad y_{j\pm\frac{1}{2}} = \frac{y_j + y_{j\pm\frac{1}{2}}}{2}$$

The subroutine `hvscrt` from the Fortran package FISHPACK (Swarztrauber and Sweet [27]) has been used to solve the equation 3.3; the solver uses the cyclic reduction algorithmn.
Cyclic Reduction has proved to be an algorithm which is very powerful for solving structured matrix problems. In particular for matrices which are (block) Toeplitz and (block) tri-diagonal, the method is especially useful. The basic idea is to eliminate half the unknowns, regroup the equations and again eliminate half the unknowns. The process is continued *ad libitum*. This simple idea is useful in solving the finite difference approximation to Poisson's equation in a rectangle.
Once the Poisson equation for the indicator function is solved we can update the fluid properties:

$$\mu_{ij} = 1 + \left(\frac{\mu_1}{\mu_2} - 1\right) H_{ij} \tag{4.9}$$

4.3 HELE-SHAW EQUATIONS SOLUTION

4.3.1 Right-end side definition

The right-end side of the adimensional Poisson equation for the pressure is composed by two terms:

RIGHT-END SIDE

$$A\delta^*(\mathbf{x}^* - \mathbf{x}_s^*) + \nabla^* \cdot \left(-\frac{1}{\mu^*} \int \kappa^* \hat{\mathbf{n}} \delta^*(\mathbf{x}^* - \mathbf{x}_f^*) ds^* \right)$$

- The injection of the inner fluid
- The divergence of the surface tension forces acting on the interface

Souce term (injection)

In our test we set

$$\delta^*(\mathbf{x}^* - \mathbf{x}_s^*) \sim \begin{cases} \delta_0(1 + cos(|\mathbf{x}^* - \mathbf{x}_s^*|\pi / r_0^*)) & |\mathbf{x}^* - \mathbf{x}_s^*| \leq r_0^* \\ 0 & |\mathbf{x}^* - \mathbf{x}_s^*| > r_0^* \end{cases} \quad (4.10)$$

where δ_0 is a normalization constant. The total injection rate is

$$A \int \int \delta^*(\mathbf{x}^* - \mathbf{x}_s^*) d\mathbf{x}^* = A\delta_0 \left(\pi - \frac{4}{\pi} \right) r_0^{*2} \quad (4.11)$$

Since we want the total injection rate to be equal to A we set $\delta_0 = (\pi r_0^{*2} - 4r_0^{*2}/\pi)^{-1}$

Surface tension treatement

The accurate computation of the surface tension is perhaps one of the most critical elements of any method designed to follow the motion of the boundary between immiscible fluids for a long time.
Here the source term in the momentum equation is treated with the conservative approach described by Tryggvason et al. [30]. The front is explicitly represented by discrete points and elements; since we explicitly track the interface using surface elements the calculation of surface tension can be performed directly on the interface.
The 'adimensional force' on a short segment of the front is given by:

$$\delta F_\sigma^* = \int_{\Delta s^*} \kappa^* \hat{\mathbf{n}} ds^*. \quad (4.12)$$

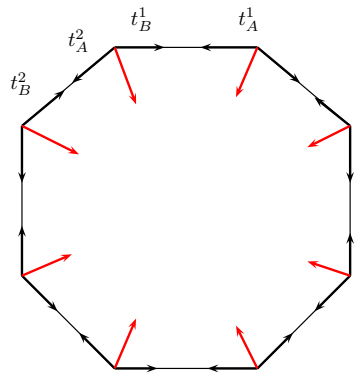

Figure 17: Conservative surface tension

Using Frenet relation, $\kappa^* \hat{\mathbf{n}} = d\hat{\mathbf{t}}/d\mathbf{s}^*$, we can write this as

$$\delta F_\sigma^* = \int_{\Delta s^*} \frac{\partial \hat{\mathbf{t}}}{\partial s^*} ds^* = t_B - t_A \tag{4.13}$$

Therefore, instead of having to find the curvature, which involves higher order derivatives and whose calculation is in general not very accurate, we only need to supply the tangents of the elements endpoints.
In addition to simplifying the computation, this ensures that the total force on any closed surface is zero since the forces on the two ends of every element cancel exactly. This conservation property is particularly important for long time computation where even a small error in the surface tension computation can lead to an unphysical net force on an interface that can accumulate over time.
The tangents are computed simply by considering the interface as made by segments connecting the interface points. Once we know the tangent for each element we simply apply the force at each element's endpoints as illustrated in figure 17. The resultant force at each endpoint is the difference of the elements' tangents.

This force must now be spread out to the grid and we have to take the divergence of the resulting force field acting on the grid. In figures 18 and 19 we have an example of the surface tension forces acting on the interface and on the grid.

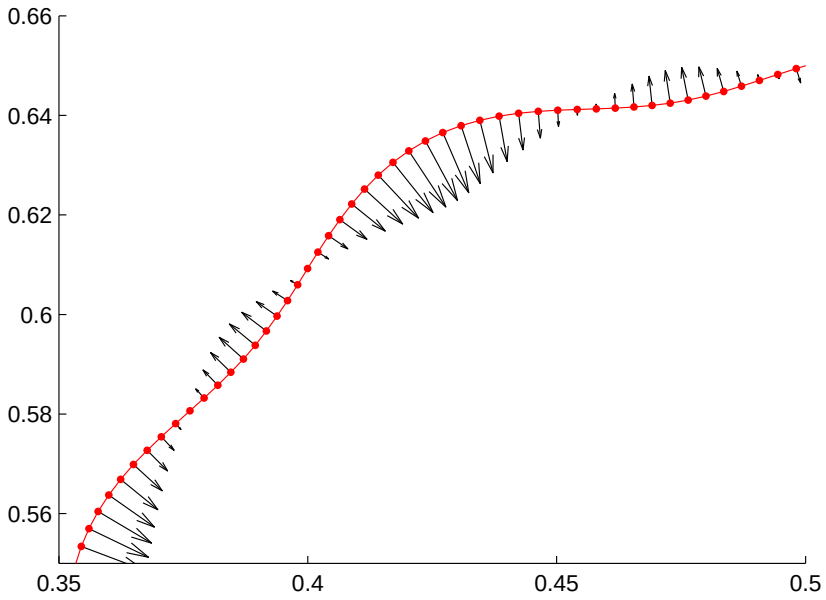

Figure 18: Surface tension forces acting on the interface

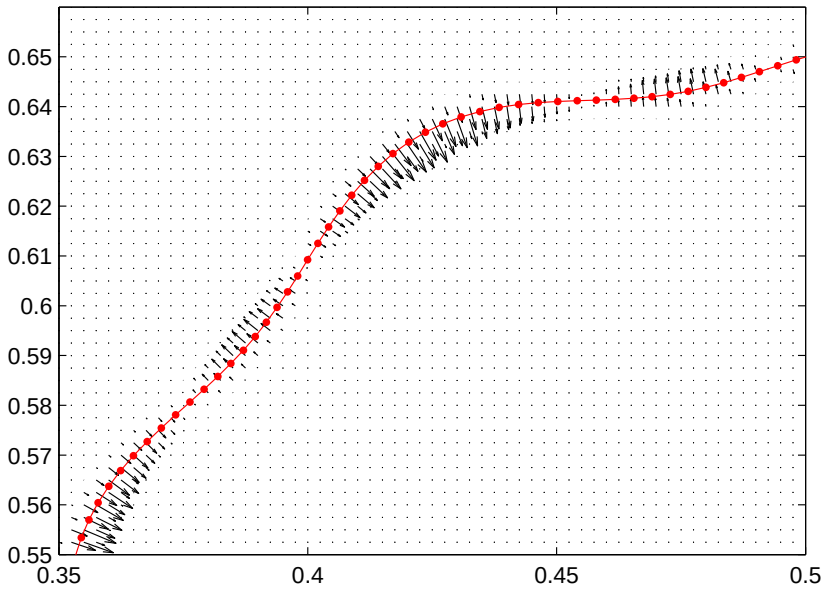

Figure 19: Surface tension forces acting on the grid

4.3.2 Pressure equation solver

Given the location of the interface at time t_n and the right-end side, we wish to to solve the Poisson equation for the pressure. We solve a difference equation of the form

$$\begin{aligned}&\frac{1}{\Delta x^2}\left[\beta_{i+\frac{1}{2},j}(p_{i+1,j}-p_{i,j})-\beta_{i-\frac{1}{2},j}(p_{i,j}-p_{i-1,j})\right]+\\&\frac{1}{\Delta y^2}\left[\beta_{i,j+\frac{1}{2}}(p_{i,j+1}-p_{i,j})-\beta_{i,j-\frac{1}{2}}(p_{i,j}-p_{i,j-1})\right]=RHS_{ij}\end{aligned}\tag{4.14}$$

on the Cartesian grid, where the coefficient β is given by

$$\beta(x^*,y^*)=-\frac{1}{\mu^*(x^*,y^*)};\tag{4.15}$$

To obtain the required values $\beta_{i\pm\frac{1}{2},j}$ and $\beta_{i,j\pm\frac{1}{2}}$ we use a double resolution for the indicator function solver ((X_I,Y_J), represented with white dots in figure 20) .

$x_i = X_{2i-1}$
$y_j = Y_{2j-1}$

Numerical simulation showed a marked grid effect with the use of the classical expressions $\beta_{i\pm\frac{1}{2},j}=(\beta_{i+\frac{1}{2},j}+\beta_{i-\frac{1}{2},j})/2$ and $\beta_{i,j\pm\frac{1}{2}}=(\beta_{i,j+\frac{1}{2}}+\beta_{i,j-\frac{1}{2}})/2$. This technique does not leat to a large increase of computational cost, thanks to the efficiency of the Fast Poisson solver for the indicator function; for this reason it has been preferred to the use of high-order interpolation formulas.
It should be noted that the resolution has been effectively doubled but this doesn't mean that the transition zone has an halved thickness: the shape of the indicator function has been kept the same of the case with the lower resolution (for consistency); this as been done using a slightly modified $\delta-$ function:

$$D_{IJ}(\mathbf{x}_p)=\delta_{/2}\left(\frac{x_p-X_I}{\Delta x}\right)\delta_{/2}\left(\frac{y_p-Y_J}{\Delta y}\right)\tag{4.16}$$

where $\delta_{/2}(r)=\delta(r)/2$.

The discretized right-end side has the following expression:

$$\begin{aligned}RHS_{ij}=&A\delta_{i,j}+\\&\frac{1}{\Delta x}\left[\beta_{i+\frac{1}{2},j}\left(ST_x\right)_{i+\frac{1}{2},j}-\beta_{i-\frac{1}{2},j}\left(ST_x\right)_{i-\frac{1}{2},j}\right]+\\&\frac{1}{\Delta y}\left[\beta_{i,j+\frac{1}{2}}\left(ST_y\right)_{i,j+\frac{1}{2}}-\beta_{i,j-\frac{1}{2}}\left(ST_y\right)_{i,j-\frac{1}{2}}\right]\end{aligned}\tag{4.17}$$

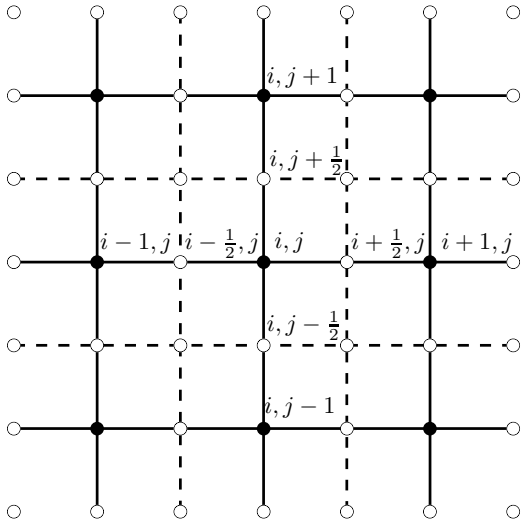

Figure 20: The double resolution grid for the indicator function

where

$$\delta_{ij} \sim \begin{cases} \delta_0(1 + cos(|\mathbf{x}_{ij} - \mathbf{x}_s|\pi/r_0)) & |\mathbf{x}_{ij} - \mathbf{x}_s| \leq r_0 \\ 0 & |\mathbf{x}_{ij} - \mathbf{x}_s| > r_0 \end{cases} \tag{4.18}$$

and

$$\mathbf{ST}_{ij} = \sum_p \mathbf{F}_{\sigma p} \frac{D_{ij}(\mathbf{x}_p)}{\Delta x \Delta y} \sim \int \kappa^* \hat{\mathbf{n}} \delta^*(\mathbf{x}^* - \mathbf{x}_f^*) ds^* \tag{4.19}$$

The numerical solution of the resulting non-symmetric system of linear equations is the major computational task in this numerical method.
The system is solved by means of a BiCG-stab algorithmn; the biconjugate gradient stabilized method is an iterative method (Krylov subspace method) developed by H. A. van der Vorst ([32]) for the numerical solution of nonsymmetric linear systems.

4.3.3 Velocity recovery

Once the pressure is known we can recovery the velocity field through:

$$\begin{cases} u_{i\pm\frac{1}{2},j} = \beta_{i\pm\frac{1}{2},j}\left[\dfrac{(\pm p_{i\pm1,j} \mp p_{i,j})}{\Delta x} - (ST_x)_{i\pm\frac{1}{2},j}\right] \\ v_{i\pm\frac{1}{2},j} = \beta_{i,j\pm\frac{1}{2}}\left[\dfrac{(\pm p_{i,j\pm1} \mp p_{i,j})}{\Delta y} - (ST_y)_{i,j\pm\frac{1}{2}}\right] \end{cases} \tag{4.20}$$

and

$$\begin{cases} u_{i,j} = \dfrac{u_{i+\frac{1}{2},j} + u_{i-\frac{1}{2},j}}{2} \\ v_{i,j} = \dfrac{v_{i,j+\frac{1}{2}} + v_{i,j-\frac{1}{2}}}{2} \end{cases} \tag{4.21}$$

Now that the velocity field is known we can compute the velocities of the interface points with the Peskin's interpolation functions with equation 4.5.

4.4 LAGRANGIAN ADVECTION

Once the velocity field has been found, the new position of the interface points can be found by integration. Note that the time evolution of the flow is governed entirely by the time dependence of the fluid properties and of the surface tension. These quantities are determined by the interface location. Once the interface location is known at a given instant in time, then the system is elliptic and the solution is determined independently of the past history of the flow. This is a reflection of the fact that there is no inertia in the system; i.e., the convective and time-derivative acceleration terms have been dropped from the momentum equations.
Equation 3.6 is advected using a Runge-Kutta method of fourth order (RK4). The coupled system of equations that must be integrated is the following:

$$\begin{cases} \dfrac{dx_p}{dt} = u_p = \displaystyle\sum_{ij} u_{ij} D_{ij}(x_p, y_p) \\ \dfrac{dy_p}{dt} = v_p = \displaystyle\sum_{ij} v_{ij} D_{ij}(x_p, y_p) \end{cases} \tag{4.22}$$

The integration scheme is the following:

```
x0 = x
y0 = y

u1 = grid2int(x0,y0,u)
v1 = grid2int(x0,y0,v)
x1 = x0 + dt/2.0d0 * u1
y1 = y0 + dt/2.0d0 * v1

u2 = grid2int(x1,y1,u)
v2 = grid2int(x1,y1,v)
x2 = x0 + dt/2.0d0 * u2
y2 = y0 + dt/2.0d0 * v2

u3 = grid2int(x2,y2,u)
v3 = grid2int(x2,y2,v)
x3 = x0 + dt * u3
y3 = y0 + dt * v3

u4 = grid2int(x3,y3,u)
v4 = grid2int(x3,y3,v)

x = x0 + dt/6.0d0 * (u1 + 2.0d0*u2 + 2.0d0*u3 + u4)
y = y0 + dt/6.0d0 * (v1 + 2.0d0*v2 + 2.0d0*v3 + v4)
```

4.4.1 Stiffness

As previously stated, surface tension is modelled by positioning a pressure jump at the interface that is proportional to the local curvature (Laplace-Joung condition). This introduces new terms into the equations of motion of the interface. Such terms have a large number of spatial derivatives. If explicit time integration is used, as is the case, here these terms may induce strong stability constraint on the time step. The presence of such constraints is referred to as *stiffness*.
Numerical experiments revealed a stability constraint on the maximum allowed time step size, which however is not dramatic.

4.5 INTERFACE RECONSTRUCTION BY LEVELS CONTOUR

Since the interface stretches and deforms greatly in our simulations, it is necessary to add and delete interface elements during the course of the calculation.
Topology change is an inherent feature of the Hele-Shaw flow, because of the pinching of fingers into droplets and also for the merging of different sections of the interface. This is crucial if we want the Hele-Shaw cell to be a good approximation of oil recovery process, wherein a fraction of the oil is left out in the form of droplets in water. Thus these droplets must be numerically reproduced, both in size and in number, to have a measure of the effectiveness of the control being studied.
In our simulations interfaces must be allowed to reconnect when either parts of the same interface or parts of two separate interfaces come close together.
The method proposed by S. Shin and D. Juric ([26]) replaces all of these (element addition/deletion and topology change) with an interface reconstruction procedure.

We take advantage of the fact that we truly have two separate representations of the interface position:

- the explicitly tracked interface elements;
- the indicator function whose 0.5 contour level also represents the interface.

Thus beginning with a given indicator function field we can deposit a collection of interface elements on the 0.5 contour or, conversely, beginning with interface elements we can solve the Poisson equation for the indicator function.
Let us suppone that at the end of a time step we have used the tracked interface elements in the solution of equation 3.3 to obtain the indicator function H at each grid point. We now completely discard the interface elements and contruct new elements.
We do this by first drawing a contour level (approximated by a line) across each grid cell at the value $H = 0.5$ using linear interpolation (a trivial slope calculation).

As shown in figure 21, the two endpoints of this contour line form the endpoints of one new interface element. Because we use linear interpolation, neighboring elements from neighboring cells will always have the same endpoint location. Since interface points that coexist at the same spatial location will move with the same velocity, the elements

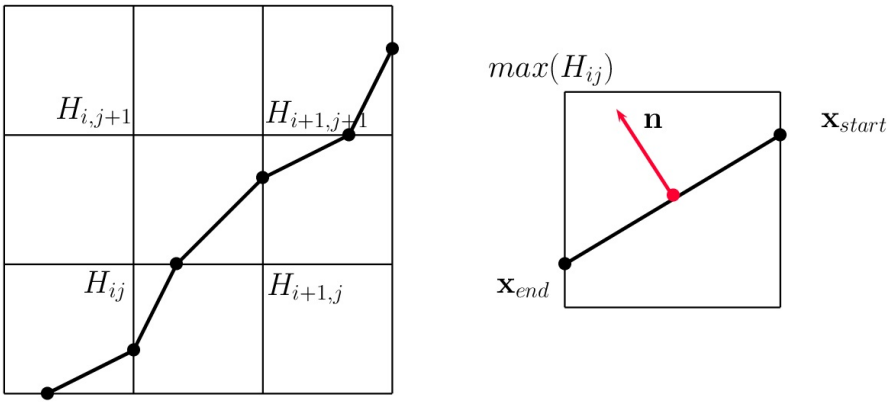

Figure 21: Level contour reconstruction. Interfaces are reconstructed by linear approximation of the $H = 0.5$ contour in each grid cell. The two endpoints of this contour line form the endpoints of one new interface elements

can never separate. Thus, although adjacent elements are not logically connected, their endpoints are automatically physically linked. In this way the adjacent interface elements are implicitly connected and the need for explicit bookkeeping of neighbor element connectivity is obviated.

For now the interface elements are arbitrarily oriented. A simple procedure is used to orient the elements so that all the elements normals point toward the inside of the volume enclosed by the surface. As shown in figure 21, the elements are oriented cell by cell such that the maximum cell indicator function value lies to the right of elements tangent drawn from point `start` to point `end`.

We now have newly constructed and properly oriented interface elements that lie on the 0.5 indicator function contour level and those endpoints are physically connected. The reconstruction step has replaced the need to add or delete single elements individually.

Most importantly, the reconstruction of interface elements from level contours of the indicator function field ensures that neighbouring interfaces reconnect when they get closer than about one or two grid cell: close interfaces can interact in a natural way since contribution to $\mathbf{N}$ in equation 4.6, calculated from the grid distribution 4.7 simply cancel. This natural interaction of close interfaces is particularly advantageous because topology changes will occur smoothly. Interface elements will be constructed with the same topological properties as the indicator function.

EXAMPLE We consider two circumferences with the same radius, externally tangent. We apply the following procedure:

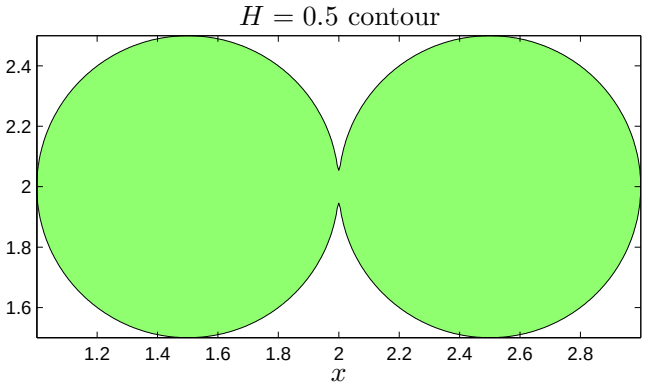

Figure 22: Merge of two interface fronts

1. Interface setup
2. Solution of equation 3.3 for the indicator function
3. Reconstruction procedure

We obtain the result reported in figure 22: we observe that a topology change occurred, as was previously explained.

For the drop pinch off case we can draw similar conclusions.
During a simulation, there is no need to carry out reconstruction at every time step; the frequency of reconstruction can be prescribed.

4.5.1 A stretching test: single vortex flow

To test our scheme on resolving thin filaments as they occur in stretching, we consider the single vortex flow. The initial interface, a circle placed at $(0.5, 0.75)$ with radius 0.15 is shown in figure 23 together with the velocity field:

$$\mathbf{u}(\mathbf{x}) = 2 \left\{ \begin{array}{c} -sin^2(\pi x)sin(\pi y)cos(\pi y) \\ sin^2(\pi y)sin(\pi x)cos(\pi x) \end{array} \right\} \tag{4.23}$$

The velocity field stretches the circle into a long filamentary structure which wraps itself around the center of the unit domain.
As the interface deforms, some parts of it are depleted of computational points, and other parts become crowded with points. To keep an adequate resolution, we must add computational elements as the interface stretches. In figure 24 the reconstruction procedure has been suppressed: the initial interface is composed by 500 poins but because of the stretching of the front this number becomes quickly inadequate. In this benchmark problem the flow field is frozen and this is the only

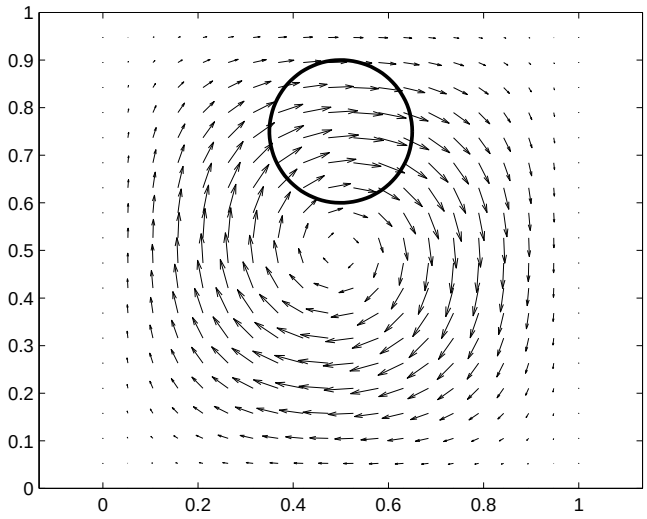

Figure 23: Single vortex flow: initial interface with velocity field

reason that allowed the computation to continue with such a marked underresolution.

In figure 39 we report a comparison between the interface at time $t = 3$ resulted from our computation with a resolution 800×800 and the one from the paper of S.E. Hieber and P. Koumoutsakos ([11]). The two fronts are indistinguishable.

A comparison between computations with different resolutions is shown in figure 26: this comparison shows that the mesh size must be chosen in order to resolve the smallest structures of interest. For example in figure 26 we observe that with the lower resolution (200×200) the scheme is not able to recover the thin filament very well.

In order to quantify the error of the method the velocity field is reversed by multiplying its value by $cos(\pi t/T)$, where T is the time of one period. For $T = 8$ the maximal stretched interface is similar to the one in figure 39. The final interface at $t = 8$ should match with the initial state. Figure 27 shows three final interfaces of this problem for three different resolutions and figure 28 shows the errors of the method in reconstructing the area as compared to the analytical solution. The errors indicate a second order convergence.

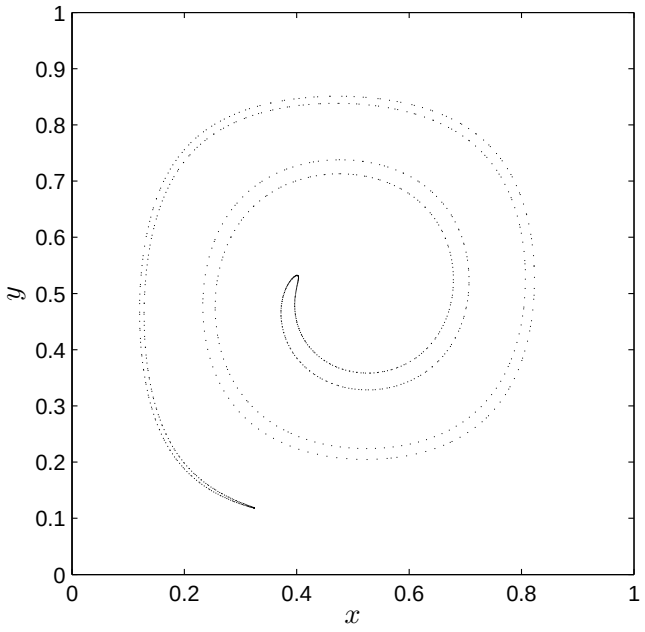

Figure 24: Interface ot the single vortex problem at $t = 3$, without reconstruction

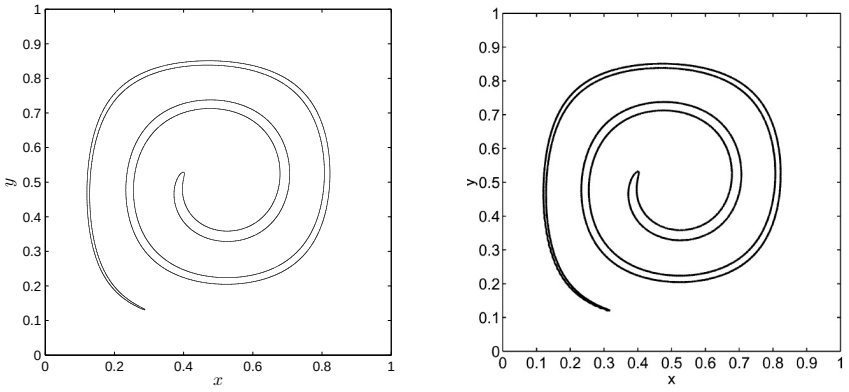

(a) *Computation by the author* **(b)** *Particle level set method*

Figure 25: Comparison between the author's computation using the front tracking method by Shin and Juric [26] with a resolution 800×800 and the one performed by Hieber and Koumoutsakos [11] using a Lagrangian particle level set method

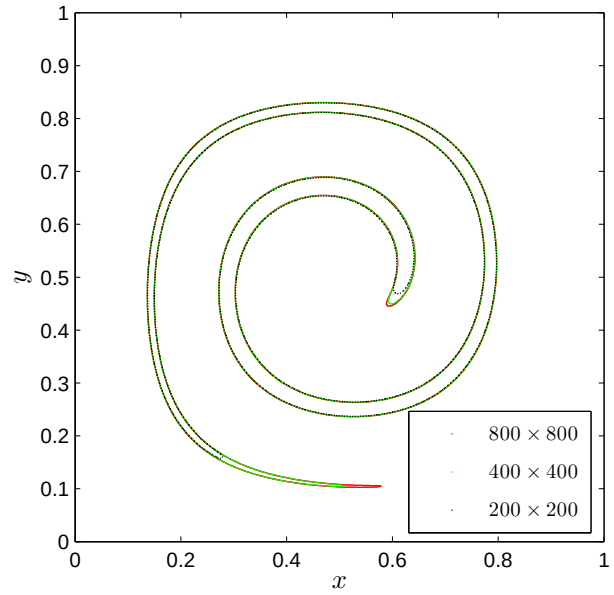

Figure 26: Comparison between computations with different resolutions ($t = 2.5$)

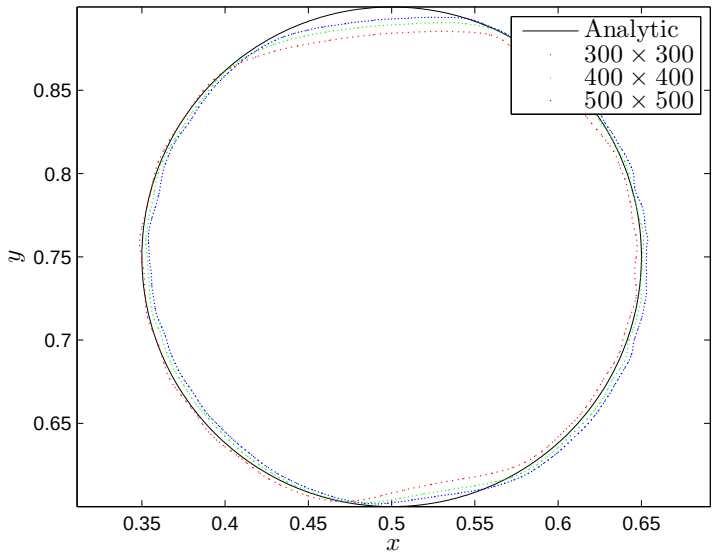

Figure 27: Time-reversed single vortex problem: comparison between some final interfaces for different resolutions

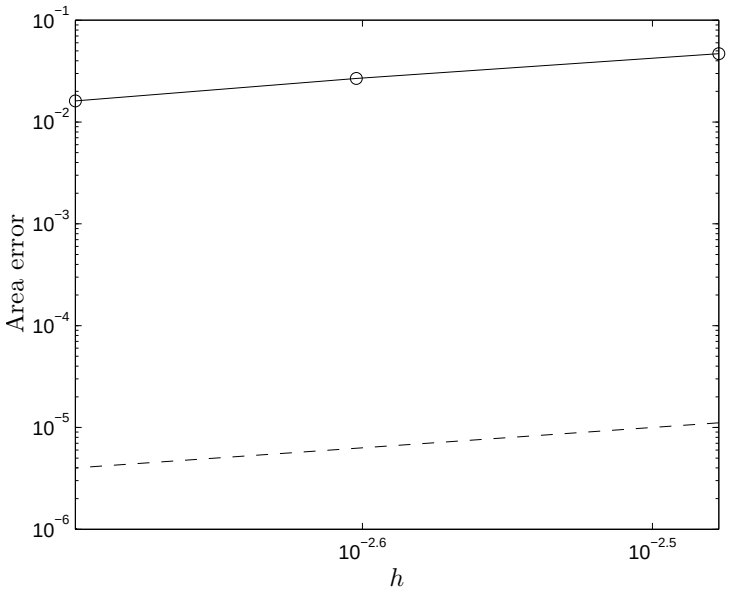

Figure 28: Comparison of the relative error of the area at $t = 8$ for three resolutions. Dotted line showing second order scaling

5 NUMERICAL EXPERIMENTS

CONTENTS

5.1 VALIDATION OF THE IMPLEMENTATION

5.1.1 Linear stability analysis

We consider the linear stability of a circular bubble perturbed azimuthally as it expands into a more viscous fluid in an unbounded Hele-Shaw cell. The circular interface is an exact solution of the governing equations, with velocity field given by

For the sake of notational simplicity in this section we omit the star apex for nondimensional variables

$$\mathbf{u}(r,t) = \frac{1}{2\pi r}\hat{\mathbf{r}}, \tag{5.1}$$

where $\hat{\mathbf{r}}$ is the radial unit vector. The radius $R(t)$ for unperturbed displacements is the solution of the ordinary differential equation

$$\frac{dR}{dt} = \frac{1}{2\pi R}, \tag{5.2}$$

that is

$$R(t) = \sqrt{\frac{S_0 + t}{\pi}} \tag{5.3}$$

The theoretical linearized growth rates of perturbations are compared to growth rates extracted from simulations.
Assume Γ is given by

$$\mathbf{R}(\theta,t) = (R(t) + \epsilon R_0 \eta(\theta,t))\hat{\mathbf{r}} \tag{5.4}$$

where $\epsilon \ll 1$ is a small parameter and $\eta(\theta, t)$ is a perturbation. Since $\eta(\theta, t)$ can be written as a Fourier series in the azimutal angle θ, and the linearized equations are separable, we consider without loss of generality a perturbation of the form

$$\eta(\theta, t) = f(n, t)cos(n\theta) \tag{5.5}$$

where n is a wave number. In section 29 it is shown that to leading order in ϵ

$$f(n, t) = e^{\sigma_n t} \tag{5.6}$$

where the instantaneous growth rate σ_n is given by

$$\sigma_n = \frac{n}{2\pi R^2}\frac{(1-\mu_1/\mu_2)}{(1+\mu_1/\mu_2)} - \frac{1}{2\pi R^2} - \frac{1}{A}\frac{n(n^2-1)}{R^3(1+\mu_1/\mu_2)} \tag{5.7}$$

We use the results of linear stability analysis as a first check of our numerical implementation. In our simulation we consider perturbations of the form in Eqs. 5.4 and 5.5 with a perturbation amplitude $\epsilon = 0.01$ and modes $n = 1, ..., 18$. For each perturbation mode n, the full equations of motion are solved for a few time steps.
For each time step we compute the location of the interface point characterized by $\theta = 0$:

$$x(t) = R(t) + a(n, t, \theta = 0) = R(t) + \epsilon R_0 f(n, t)cos(0). \tag{5.8}$$

We obtain:

$$f(n, t) = \frac{x(t) - R(t)}{\epsilon R_0} \tag{5.9}$$

Applying the logarithm to Eq. 5.6 we have $log[f(n, t)] = \sigma_n t$, so that we can compute the growth rate with the formula

$$\sigma_n = \frac{log[f(n, t)]}{t} = \frac{1}{t} log\left[\frac{x(t) - R(t)}{\epsilon R_0}\right] \tag{5.10}$$

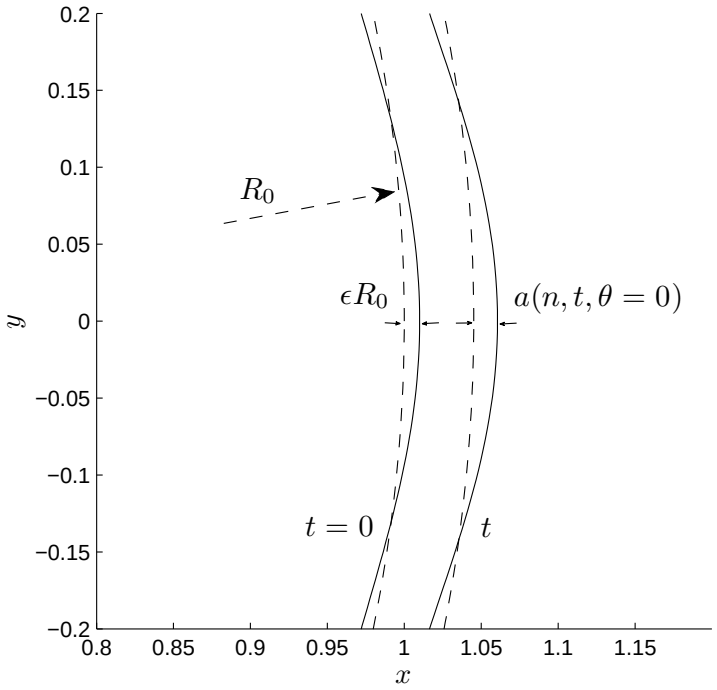

Figure 29: Linear stability analysis nomenclature

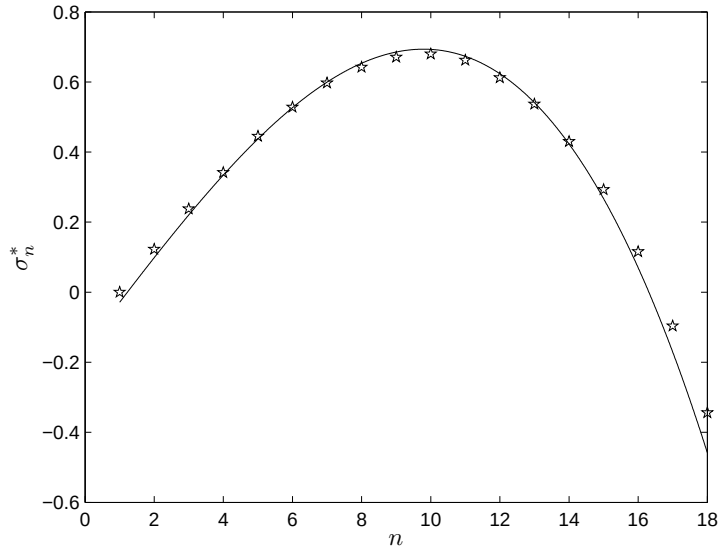

Figure 30: Comparison of the analytic result to linear growth rates from the front tracking code with $A = 2 \cdot 10^3$, $\mu_1/\mu_2 = 0.1$ and $R_0 = 1$

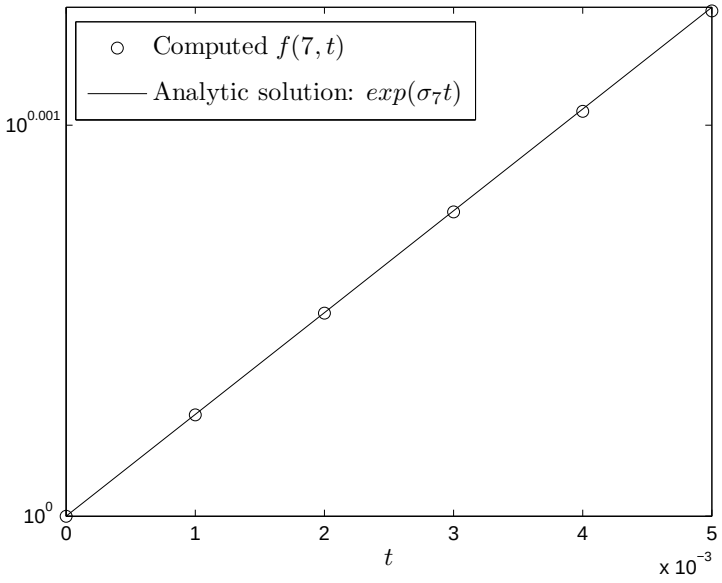

Figure 31: Comparison of the analytic result to $f(n,t)$ from the front tracking code with $A = 2 \cdot 10^3$, $n = 7$, $\mu_1/\mu_2 = 0.1$ and $R_0 = 1$

Comparison

In figure 30 we compare the analytic linear growth rates from equation 5.7 with growth rates obtained with the code for a case with $A = 2 \cdot 10^3$, $\mu_1/\mu_2 = 0.1$ and $R_0 = 1$. The resolution adopted is 500×500 and the domain is 5×5. We used a time step $\Delta t = 0.001$.

The agreement between theory and simulations is good, though for large wavenumbers, the growth rates from linear theory have slightly smaller absolute amplitudes than the growth rates from the simulations. However, the large wavenumber behaviour is strongly dissipative in the problems considered here and has little effect on the simulations as long as the wavenumbers with positive growth are resolved. It is well known that finite differences schemes do not capture high frequency phenomena accurately, so it is important to resolve the length scales of interest as has been done here.
In figure 31 we can observe a comparison between $f(n,t) = e^{\sigma_n t}$ with σ_n obtained from equation 5.7 and $f(n,t)$ calculated from equation 5.9. The results, for the case with $n = 7$, are plotted with logarithmic scale for the y-axis so that we can see two overlapping straight lines.

REMARK It is standard practice in boundary integral simulations of interfacial instabilities to present numerically computed linearized growth rates and compare those to analytical results as has been done in this section (Hou, Lowengrub, and Shelley [14]). How-

ever, in simulations of interfacial instabilities using finite differences and finite elements methods, it is unfortunately uncommon to present such results. Since the linear instabilities are at the heart of many interfacial instabilities, it is important to discuss the fidelity of the numerical scheme in capturing this key feature of the physical problem.

5.2 SIMULATIONS OF THE SAFFMAN-TAYLOR INSTABILITY

We have carried out a number of numerical experiments with different initial interfaces, viscosities and surface tensions.
All results seems to agree with the theoretical analysis and numerical results available in the literature.
Since the Hele-Shaw flow is unstable for long time computations, the results do not converge to a unique solution due to the roundoff and the discretization errors. This is consistent with experiments in which different shapes are observed after some time. However, this should not invalidate our simulations because we still can predict roughly the shape and location of the interface as time evolves. Moreover, for a short time period, the solution does converge and the computational result is independent of the grid.
The crucial parameter which affects the stability is the surface tension parameter $A = 12\mu_2 Q/(\sigma b)$. The larger the parameter A, the more unstable the Hele-Shaw flow.
The basic elements of a pattern formation for a bubble expanding in a radial Hele-Shaw cell are well understood from experiments (Paterson [21], Lajeunesse and Couder [17]) and careful numerical simulations (Hou, Lowengrub, and Shelley [15], Hou et al. [16], Li, Lowengrub, and Leo [19]).
Very roughly, a perturbation of the bubble interface grows outwardly into an expanding petal. When this petal's radius of curvature exceeds the wavelength of an unstable mode, it tipsplits into two nascent petals, which themselves broaden and split. This repeated process yields an interface described by a population of branches and fjords, and whose evolution is characterized by strong competition among the branches, with some branches being shielded and retracting, and others advancing further into the fluid. We consider the evolution of the interface at different values of the surface tension parameter A; as initial data we take

$$(x_0(\theta), y_0(\theta)) = r(\theta)(cos(\theta), sin(\theta)), \tag{5.11}$$

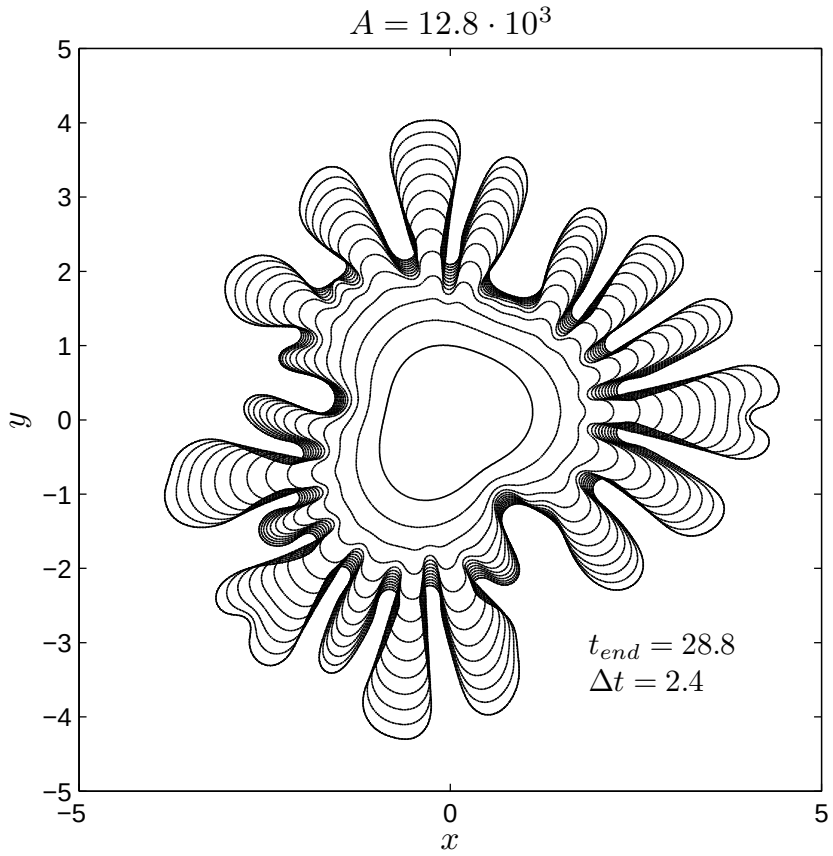

Figure 32: An expanding Hele-Shaw bubble with initial interface $r(\theta) = 1 + 0.1(cos(3\theta) + sin(2\theta))$ and $A = 12.8 \cdot 10^3$

where

$$r(\theta) = 1 + 0.1(cos(3\theta) + sin(2\theta))$$

as in Hou, Lowengrub, and Shelley [15], so that no particular symmetry on the ensuing motion is imposed. In all cases the initial data are unstable to Saffman-Taylor instability.

Figure 32 shows the expansion of the bubble from $t = 0$ up to $t = 28.8$, at equally spaced intervals of time. The value of the surface tension parameter is $A = 12.8 \cdot 10^3$ and the viscosity ratio $\mu_1/\mu_2 = 0.02$. A 500×500 grid has been used and the time increment is $\Delta t = 0.01$. This simulation displays much of the behaviour that has stimulated interest in pattern formation in Hele-Shaw flows. At early times, three main fjords form in the interface; these fjords separate three expanding fronts. The number of fjords arises from the $n = 3$ component in the initial data. The expanding fronts rapidly develop oscillations which themselves form fingers and petals.

The petals expand outwards and eventually tipsplit into two petals.

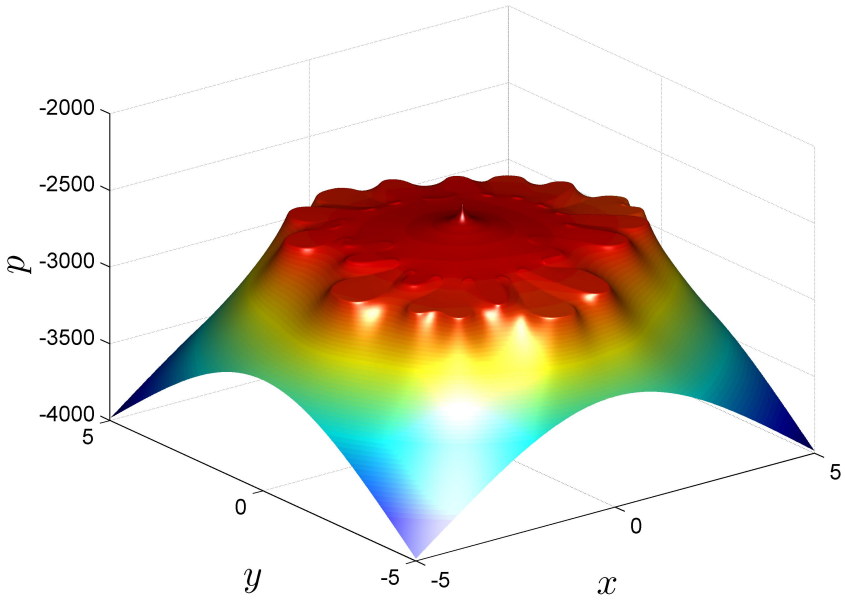

Figure 33: Pressure field at $t = t_{end}$ for the case with $A = 12.8 \cdot 10^3$

There is also abundant evidence of competition between these various structures. Of the approximately 20 protuberances that develop at early times, only about 15 of them are still actively growing outwards as $t = 28.8$. The remainder have either stopped growing outwards, or have receded and been absorbed back towards the main bulk of the bubble.

In figure 33 we can see the pressure field at $t = t_{end}$. We observe that the pressure is approximately constant in the zone of lower viscosity, as follows from equation 2.3 if we neglet viscosity ($\mu_1/\mu_2 = 0.02$).

Figure 34 shows the isolines of the velocity field modulus: there are regions of high velocity in the necks which connect the longest fingers to the 'mother' fluid because the fluid is forced to pass into a narrow corridor. We observe that the isolines thicken in proximity of the fjords: in fact the velocity at the fjords is very low, and this implies that there must be a zone of high velocity gradients where the velocity passes from his characteristic value to a value close to zero. Similar conclusion can be drawn for the tips of the fingers, where we have a velocity surplus which allows the fingers to grow.

Figure 35 shows the streamlines of the velocity field: the fjords behave approximately like stagnation points, and the inner fluid is forced to pass through the fingers, which consequently have to grow.

Figure 36 shows the bubble area $S(t)$ versus the radius of gyration $G(t)$ on a log-log scale. $G(t)$ is defined as the maximum distance of

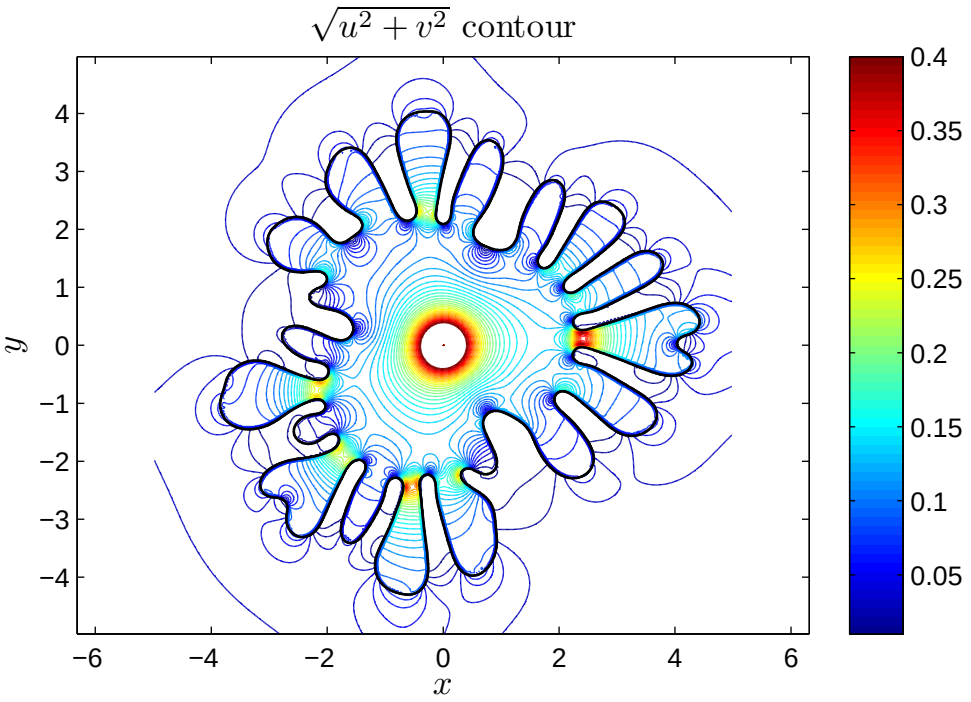

Figure 34: Isolines of the velocity field modulus at $t = t_{end}$ for the case with $A = 12.8 \cdot 10^3$

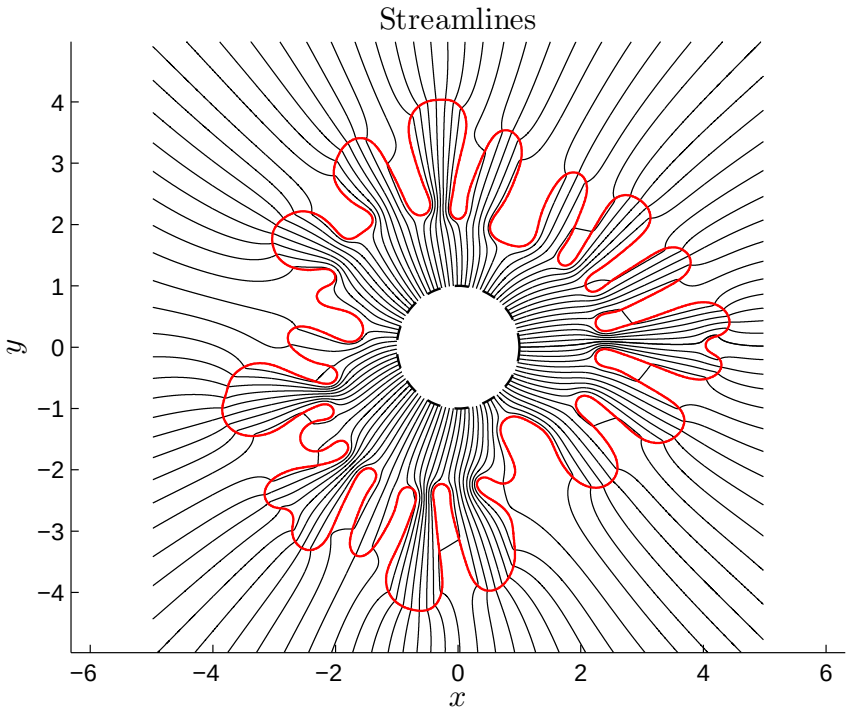

Figure 35: Stream lines at $t = t_{end}$ for the case with $A = 12.8 \cdot 10^3$

a point on the interface from the injection point. The radius of gyration has been used as a measurement of complexity, as the slope of $logG$ versus $logS$ gives roughly a dimension d, where d is the dimension of the bubble (i.e. $S \sim G^d$). For example the slope is two for a circular bubble. This slope is, of course, not smooth, as the point of maximum radius jumps between different sites during the evolution. The jumps themselves are associated typically with tip-splitting events, as the splitting allows a newly formed finger to move outwards more quickly. The slope of $logG$ versus $logS$ as a function of time is plotted in figure 37: the dashed lines have the values 1.71 and 1.66 (see and respectively), which are estimates for the fractal dimension of a branched object grown via diffusion limited aggregation (DLA), a prototypic model for the growth of branched structures (Zhang, Luo, and Liu [34]). There is a period ($14 < t < 25$) of good agreement with these values, but the behaviour of the slope is mostly characterized by large deviations from these values. The noise is due to numerical errors that emerge while differentiating and expecially to the interface reconstruction procedure.

The area is computed using the very simple *shoelace formula*, which applies perfectly to the method we used, in which adjacent interface elements are not logically connected:

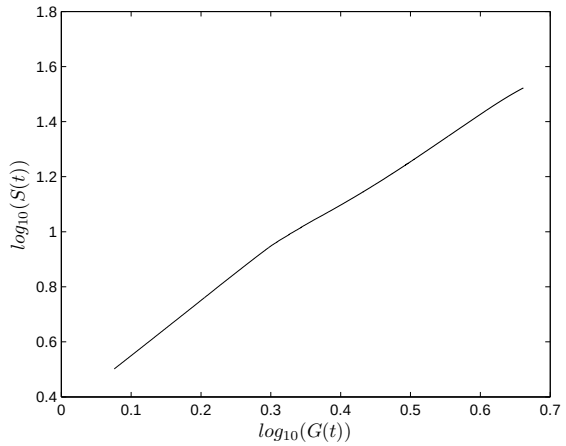

Figure 36: The bubble area $S(t)$ vs the radius of gyration $G(t)$ on a log-log scale

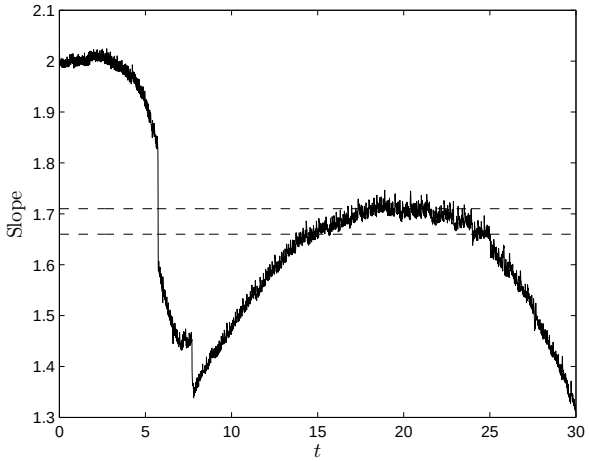

Figure 37: Slope (dimension) d measured from figure 36 as a function of time

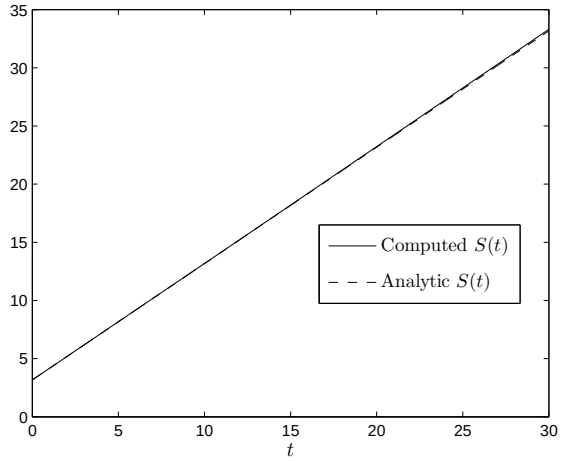

Figure 38: Analytic and computed bubble area vs time

```
p_area = 0.0d0

do i = 1,np
p_area = p_area + (xend(i) + xstart(i))*(yend(i) - ystart(i))
enddo

p_area = abs(p_area)/2.0d0
```

Figure 38 shows the comparison between the analytic bubble area as a function of time and the one computed during the simulation; we can observe a satisfactory agreement between the two, so that we considered not necessary to implement a technique that improves the mass conservation during the reconstruction procedure (Shin and Juric [26]).

The expanding fronts develop more fingers and petals depending on the ratio between surface tension and mass inflow. For large values of this ratio, only a few low frequencies are unstable for each fjord. As we decrease the ratio, more Fourier modes become unstable and we see more fingers and petals, see figure 39. For a short time, the shape of the interface varies little for different values of the surface tension parameter. The bigger the surface tension parameter, the quicker the secondary structure develops. As we decrease the physical surface tension further, the numerical dissipation becomes more apparent, indicating the limitation on the real surface tension that we can resolve.

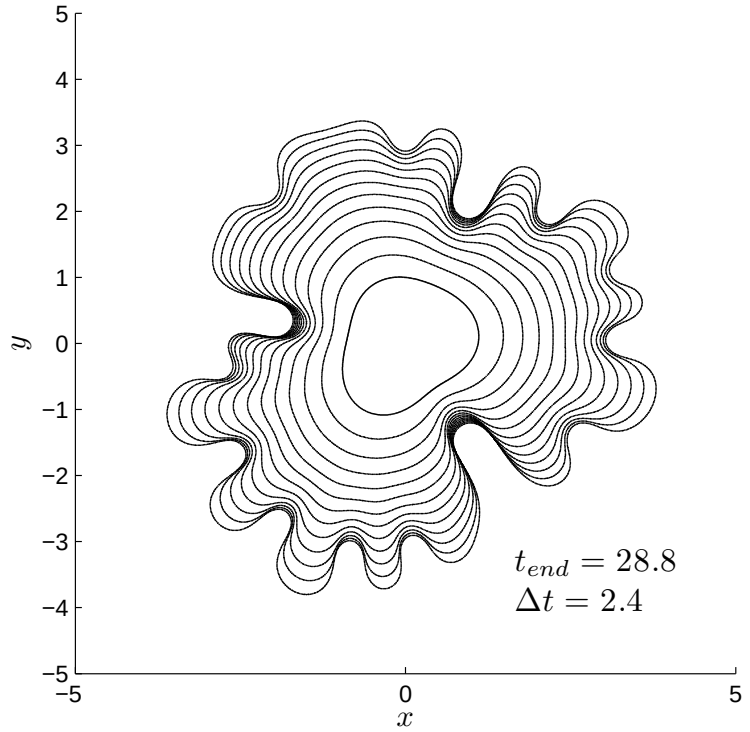

(a) $A = 3.2 \cdot 10^3$

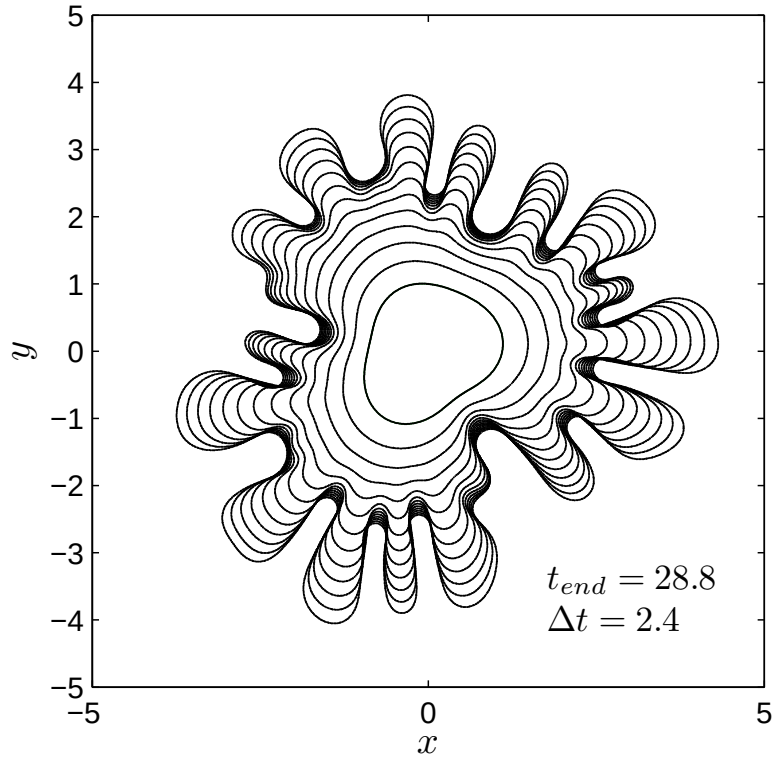

(b) $A = 6.4 \cdot 10^3$

Figure 39: Bubble expansion comparison between the cases with $A = 3.2 \cdot 10^3$ and $A = 6.4 \cdot 10^3$

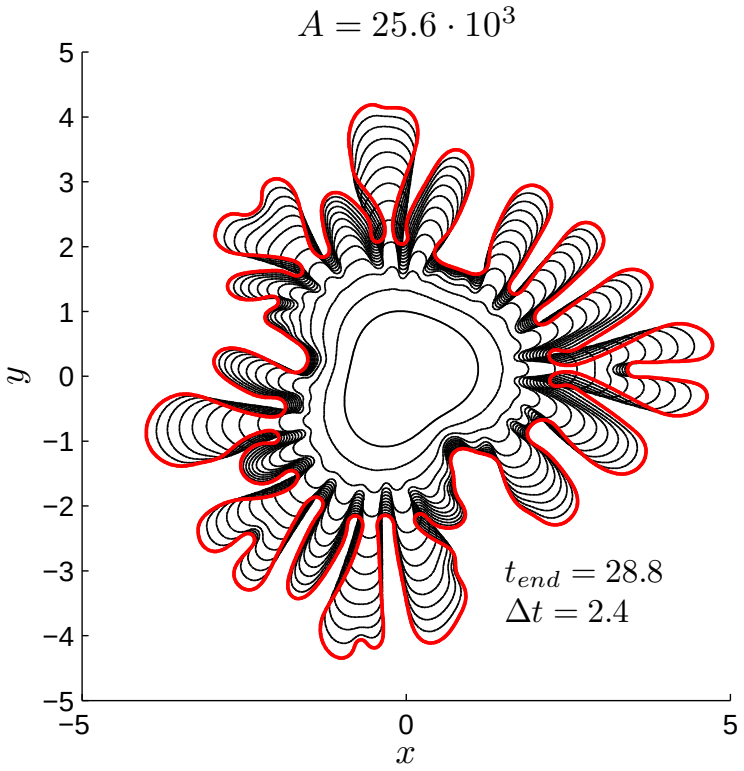

Figure 40: An expanding Hele-Shaw bubble with initial interface $r(\theta) = 1 + 0.1(cos(3\theta) + sin(2\theta))$ and $A = 25.6 \cdot 10^3$

5.2.1 A case with topology change

In order to investigate the effect on the evolution of the interface of larger viscosity ratios a run was performed with $A = 25 \cdot 10^3$. The result is shown in figure 40: at later times the longest fingers produce a bubble at the end connected to the mother fluid by a long and narrow neck. These structures are similar to those reported in Tryggvason and Aref [29], see figure 41.

If we take some steps forward in the simulation we find out that these bubbles detach and propagate into the more viscous one. Figure 42 shows the evolution of one of these bubbles. When the neck becomes very thin, the two parts of the interface approach closer than about one or two grid cells and contributions to **G** in equation 4.6 simply cancel; since the level contour reconstruction technique uses contours of indicator function to create interface elements, these latter are constructed with the same topological properties as the indicator function and consequently at a certain time the bubble detaches.

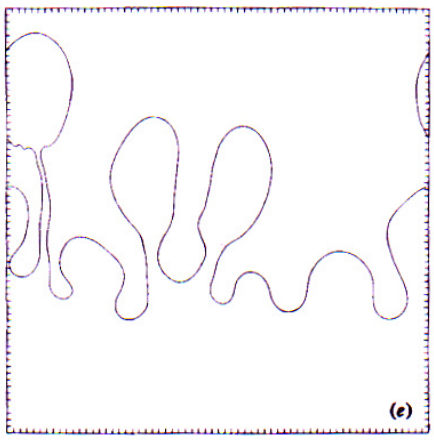

Figure 41: Density driven viscous fingering, computation by Tryggvason and Aref [29]

This run gives an effective example of the competition between the fingers: the neck becomes thinner and thinner because of the expansion of the neighbouring structures; when the interface breaks, the structure below is drawn into the detached bubble (figure 42, (d)) and when it gets too close the two interface parts merge to form a unique structure (figure 42, (e)).

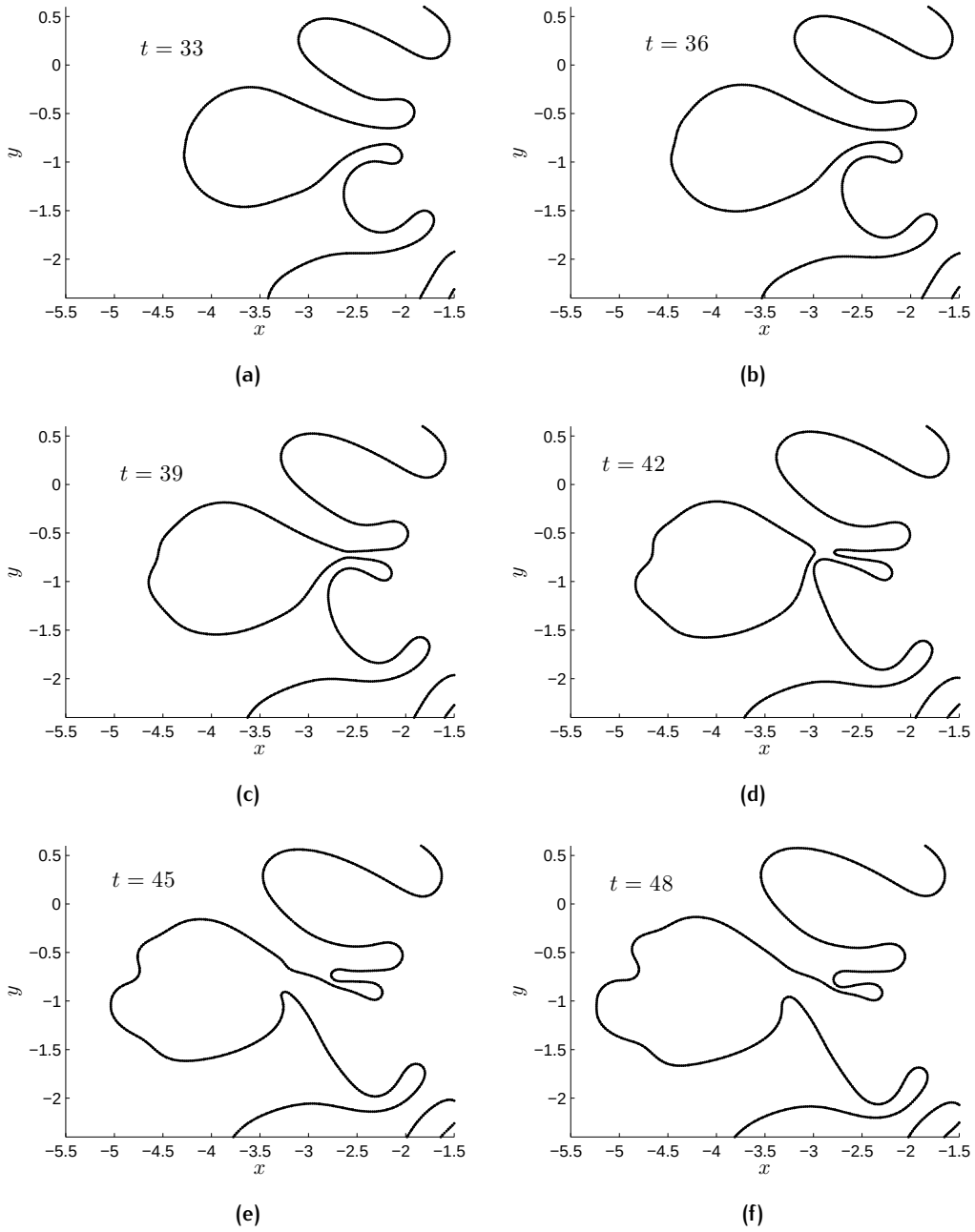

Figure 42: The process of bubble detachment and reattachment

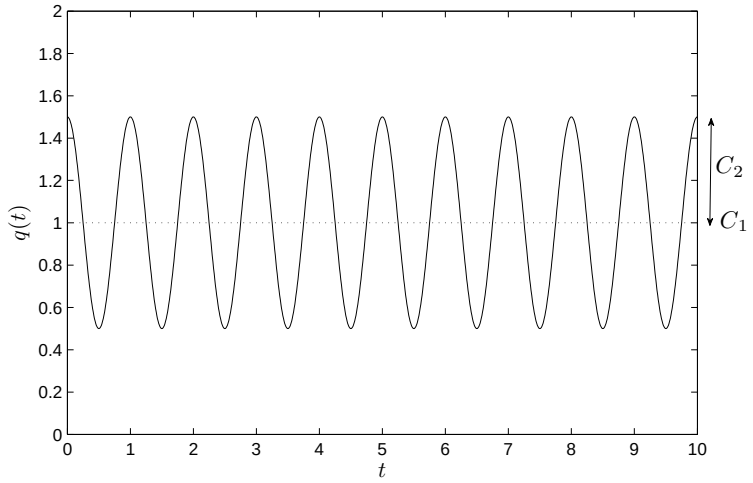

Figure 43: Unsteady pumping

5.3 UNSTEADY PUMPING

As was previously explained the ultimate goal of this work is to verifiy the possibility of selectively suppress some unstable wavenumbers in order to hinder the development of the fingering pattern.
To do that we simulate the response of the system to an unsteady forcing (mass inflow) composed by a static part and a superimposed armonic component. We run a number of cases in a broad band of frequencies and amplitudes.
We hope that for certain combinations of frequencies and amplitudes of the armonic part of the forcing, the growth of the interface perturbations is dumped and the extent of fingering reduced.
We have to pay some attention during the adimensionalization of the equations because it can lead to errors. Continuity equation for an unsteady pumping is the following:

$$\nabla \cdot \mathbf{u} = Q(t)\delta(\mathbf{x} - \mathbf{x}_s) \tag{5.12}$$

where we write $Q(t)$ as

$$Q(t) = Q_0 q(t) = Q_0 \left[C_1 + C_2 cos(2\pi f_{pump} t)\right]. \tag{5.13}$$

The adimensional inflow $q(t^*)$ is plotted in figure 43.

We define the adimensional velocity using a typical value of $Q(t)$, that is Q_0:

$$\mathbf{u}^* = \frac{\mathbf{u}}{U_R} = \frac{\mathbf{u}}{Q_0/b}$$

The adimensional mass conservation equation is:

$$\nabla^* \cdot \mathbf{u}^* = q(t^*)\delta^*(\mathbf{x}^* - \mathbf{x}_s) \tag{5.14}$$

For p, $\mathbf{x}$, μ, δ and κ we use the same adimensionalization introduced in 3.2. We obtain

$$\mathbf{u}^* = -\frac{1}{A}\frac{1}{\mu^*}\left(\nabla^* p^* - \int \kappa^* \mathbf{n}\delta^*(\mathbf{x}^* - \mathbf{x}_f^*)ds^*\right) \tag{5.15}$$

where the adimensional parameter A is now

$$A = \frac{12\mu_2 Q_0}{\sigma b}.$$

Applying the divergence to equation 5.15 and using equation 5.14 we obtain

$$\begin{aligned}\nabla^* \cdot \left(-\frac{1}{\mu^*}\nabla^* p^*\right) =& Aq(t^*)\delta^*(\mathbf{x}^* - \mathbf{x}_s^*) \\ &+ \nabla^* \cdot \left(-\frac{1}{\mu^*}\int \kappa^* \mathbf{n}\delta^*(\mathbf{x}^* - \mathbf{x}_f^*)ds^*\right)\end{aligned} \tag{5.16}$$

The adimensional boundary condition for the case with unsteady pumping is

$$p^*(R_{out}^*) = -A\frac{q(t^*)}{2\pi}log(r^*) \tag{5.17}$$

5.3.1 A first attempt at fingering control

We have seen previously that the competition between fingers can lead to a break-up of the interface in multiple points. We have also highlighted the characteristic behaviour associated with a bubble detachment: the neighbouring fingers are drawn into the detached bubble and they merge to form a unique structure.
Bubble detachment can be positive from the point of view of the control because it causes the rupture of the coherence of the fingering pattern. In this perpective the reattachment must be avoided because it would allow the structure to continue her growth.
Figure 44 shows the pinchoff of a bubble when, starting from a developed fingering, we force the system with an armonic mass inflow $q(t)$ with $C_2 = 10$ and $f_{pump} = 1/3$.

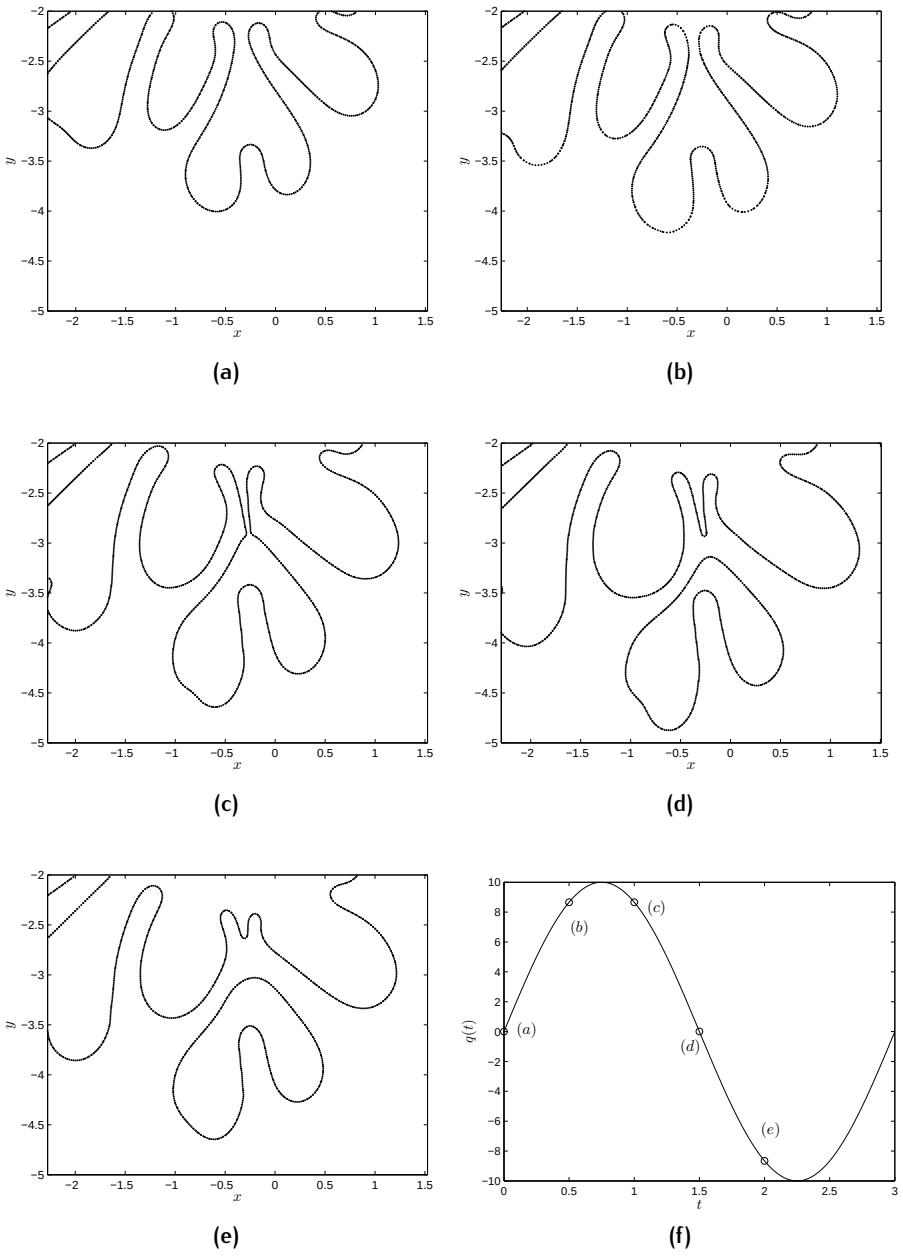

Figure 44: Pinchoff of a bubble due to an armonic forcing

A number of simulations in a broad band of frequencies and amplitudes have been carried out. Particularly we tested the response of the system to an unsteady forcing composed by a static part ($C_1 = 1$) and a superimposed armonic component, starting from the initial interface defined by equation 5.11. The frequencies range from $1/T$ to $100/T$ and the amplitudes C_2 range from 0.02 to 2. The final time is $T = 30$, as in the examples presented previously. We obtained 15% reduction (maximum) of the fingering extent (measured as the maxiumum distance from the injection point) for the combination $f_{pump} = 3/T$, $C_2 = 0.2$.

6 CONCLUSIONS AND FURTHER STUDIES

A robust method for the numerical simulation of viscous multiphase flows in two dimension has been implemented.
We have addressed our attention to the study of radial viscous fingering in a Hele-Shaw cell, for which interface merging/breakup is a predominant feature.
The heart of the method is a simple technique for reconstructing the phase interface from a level contour of the indicator function. All of the accuracy and advantages of explicit Lagrangian interface tracking are retained, while the complexity of mantaining logical connectivity of the interface mesh is eliminated.
The reconstruction method accomplishes the operations of interface element addition, deletion and reconnection simultaneously in one step. Interface merging/breakup is performed naturally and automatically since the newly constructed surface elements take on the same topological properties as the indicator function.
We have conducted numerous validation tests, finding good agreement with the linear stability analysis theory and with non linear results from previous computations.
Our simulations highlight competition between fingers, which can cause a particular behaviour of the interface with consecutive detachments and reattachments of interface pieces.
The robustness of this method is very attractive because it allows to simulate flows in realistic configurations for petroleum engineering; for example configurations with multiple injection points and/or with the addition of extraction points can be considered.
A very first attempt at fingering control has been done, testing the response of the system to an armonic pumping, which allows bubbles to detach, avoiding the consequent reattachment. This result is interesting because it can cause the rupture of the coherence of the fingering pattern, suppressing the growth of some of its parts. A 15% reduction of the fingering extent has been observed, superimposing an armonic pumping to a static one, for a certain combination of frequencies and amplitudes.
The simulations presented here use relatively high resolution grids of 500^2 up to at most 700^2[1]. Computations with a steady pumping can

1 Remark: for the indicator function double resolution grids are used, i.e. grids of 1000^2 up to 1400^2.

be done within $4-5$ hours on a *Intel®Core^{TM}i7 CPU @ 2.00 GHz*. Calculations with unsteady pumping are more computationally expensive and the cost depends on the variability of the forcing. We have as of yet not fully optimized the code or tested the code on more advanced or parallel architectures.
We believe that the actractiveness out this simulation tool lies in its combination of accuracy and robustness.

A THE CODE

The code is implemented in *Fortran 90*. In this appendix a short explaination of its structure will be given.
The program receives some input parameters which are divided into two categories:

- Static input parameters (e.g. resolution, dimensions of the domain, frequency of output production/interface reconstruction), t_{max}, etc... ; these input parameters are contained in the file `data.dat` (tab. 1)
- Dynamic input parameters: frequency and amplitude of the armonic component of the forcing, which are dynamically generated from a test matrix. These input parameters are contained in the file `input.dat`

The standard output is represented by the locations of the interface segments at a certain time, which are written into files named for example `interface_loc_17.dat`, where the number indicates a progressive counter. Files with velocity, pressure or viscosity fields can also be produced.

The code is divided into the following parts, each of which is packaged into a *module*:

Table 1: Input file

M,N	Resolution (x and y)
x_{max}, y_{max}	Domain dimensions
r_0	Radius of the initial interface
μ_1/μ_2	Viscosity ratio
A	Surface tension parameter
C_1	Stationary component of $q(t)$ (usually 0 or 1)
Δt	Time increment
f_{rec}, f_{plot}	Frequency of reconstruction/data writing
n_{sin}, n_{cos}	Wavenumbers of the azimuthal perturbations of the initial interface
A_{sin}, A_{cos}	Amplitudes of the azimuthal perturbations of the initial interface
r_{lim}	Threshold of the residual (BiCG-stab)
`flag`	New/old computation
t_{max}	Maximum time
`path`	Name of the folder where to write data

MAIN PROGRAM The main program is contained into the file `driver.f90`. It contains calls to subprograms and the `DO` loop in time.

VARIABLES DECLARATION Global variables are declared in the file `var.f90`. Every subroutine make use of these global variables thanks to the statement `USE var`. Some arrays must be dynamic in nature; these are handled in *Fortran 90* using the `allocatable` modifer during declaration.

INPUT FILE READING AND PARAMETERS DEFINITION These operations are managed by the module `def_par.f90`. This module contains the subroutines `read_input_file()` and `define_parameters()`.

INITIALIZATION The module `init.f90` contains all the initialization routines:

- Grid generation, performed by the subroutine `grid_gen()`, which generates the two grids of figure 20
- Interface setup: this operation is managed by the subroutine `interface_setup()` if the input variable `flag` is equal to `0` or by the subroutine `resume_data()` if `flag = 1`. In the first case the desired initial interface is generated by defining the arrays `xstart`, `ystart`, `xend` and `yend`; in the second case a stopped computation is restarted by reading the last output file `interface_loc_XX.dat` produced

FAST POISSON SOLVER All the subroutines from the package FISHPACK necessary for the solution of equation 4.6 are contained in the module `fps.f90`

INTERFACE TRACKING The module `intrack.f90` contains all the subroutine which concern the interface tracking method and particularly the subroutine `rhsH(rhs)` which define the right-end side of equation 4.6, the subroutine `PoissonH(ff)` which calls `hwscrt` from the FISHPACK package and defines all its inputs and lastly the subroutine `DetermineIntFace()`, which carries out the interface reconstruction procedure described in 4.5.

HELE-SHAW EQUATIONS SOLVER The subroutines necessary for solving the Hele-Shaw equations can be found in the module `HS.f90`. These subroutines are:

- `surface_tension(STx_poh,STx_moh,STy_poh,STy_moh)`, which computes the surface tension as described in 4.3.1.
  `STx_poh`, `STx_moh`, `STy_poh`, `STy_moh` represent respectively $(ST_x)_{i+\frac{1}{2},j}$, $(ST_x)_{i-\frac{1}{2},j}$, $(ST_y)_{i,j+\frac{1}{2}}$ and $(ST_y)_{i,j-\frac{1}{2}}$ from equation 4.17;

- `rhs()`, which calls `surface_tension(STx_poh, STx_moh, STy_poh, STy_moh)` and build the right-end side of the equation for the pressure, as described in 4.3.1;
- `rhs_boundary()`, which applies the changes to the right-end side due to the Dirichlet boundary conditions; it is called by `rhs()`;
- `dirichlet_BC()`, which defines the value of the pressure on the boundary, as specified in equation 3.2
- `press_solver()`, which calls `rhs()` and solves the linear system defined by 4.14 with the BiCG-stab algorithmn;
- `compute_grid_vel()`, which computes the velocity of the interface points from the values of the pressure, as explained in 4.3.3

UPDATE OF THE FLOW PROPERTIES Once the indicator function H_{ij} is known, the flow properties (in terms of viscosity) are updated using the definition 4.9 and the coefficient β, defined by equation 4.15, is built by the subroutines `mu_setup()` and `coeff()`, which are contained in the module `upd.f90`.

INTERFACE ADVECTION Once the velocity field has been computed one can advect the interface points thanks to the subroutine `int_advection()`, which calls `grid2int()` for the interpolation from the grid to the interface, as explained in the section 4.4.

WRITING ON FILE At last, every f_{plot} times, some output files can be produced, containing the location of the interface points at a fixed time and eventually the pressure/velocity/viscosity fields.

B HELE-SHAW CELL FOR FLOW VISUALIZATION

It is by now a standard textbook fact (Batchelor [4], Acheson [1]) that Hele-Shaw cells can be used as an apparatus for visualizing the streamline pattern of two-dimensional Euler flows of an ideal fluid past an obstacle (figure 45).

Indeed, such a visualization constitutes the very first photograpf in van Dyke's *Albun of fluid motion*[31] and it is annotated with the comment that *'It is at first sight paradoxical that the best way of producing the unseparated pattern of plane potential flow past a bluff object which would be spoiled by separation in a real fluid of even the slightest viscosity, is to go to the opposite extreme of creeping flow in a narrow gap, which is dominated by viscous forces'*.

These unexpected similarities between two very different physical problems do not seem quite so unexpected when one writes down the mathematical problem statement in each case. Indeed, after the various approximations and assumptions, in the bulk fluid both Euler flow and Hele-Shaw flow reduce to a Laplacian field equation for a velocity potential ϕ with the fluid velocity given as $\mathbf{u} = \nabla\phi$, i.e. the problems are kinematically equivalent.

The essential difference between the problems is dynamical in nature: in the Hele-Shaw problem, the pressure $p(x, y)$ in the fluid is linearly related to the potential function via

$$p(x, y) = -\frac{12\mu}{b^2}\phi \tag{B.1}$$

while for steady potential flows, integration of the Euler equations yields Bernoulli's theorem which states that the fluid pressure $p(x, y)$ is given as a nonlinear function of the velocity potential via the condition that

$$p + \frac{|\mathbf{u}|^2}{2} = p + \frac{\phi_x^2 + \phi_y^2}{2} \tag{B.2}$$

is constant on streamlines.

For this reason, as soon as one starts to consider free-surface problems in which the fluid pressure usually enters the boundary conditions explicitly, one no longer anticipates any kind of connection, either physical or mathematical, between Euler and Hele-Shaw flows.

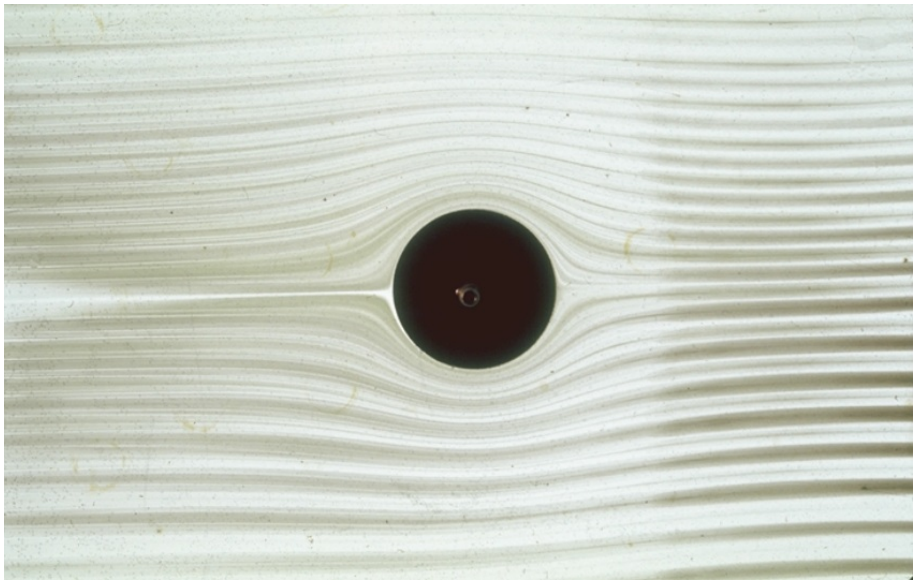

Figure 45: Visualization of the flow around a cilinder with an Hele-Shaw apparatus

One must notice however that the boundary condition on the wall is necessary different between the Euler and the Hele-Shaw flow: 'no-flow' condition in the first case and 'no slip' condition in the second case. This means that the streamlines of the two flows, even if hardly discernible, are only apparently similar.

C GRAVITY DRIVEN HELE-SHAW CELL

Here we present the equations for the motions of bubbles through an immiscible liquid under the effect of gravity(see also LeVeque and Zhilin [18]). The physical setup is the same presented in chapter 3, except for the fact that the Hele-Shaw cell is now vertical and gravity must be taken into account. A version of the code which deals with the effect of gravity has been written with few modifications compared to the standard version.

C.1 BUBBLES RISING

C.1.1 Governing equations

If we add gravity to equation 3.14 we have:

$$\mathbf{u} = -\frac{b^2}{12\mu}\left(\nabla p - \int_{\Gamma(t)} \sigma\kappa\hat{\mathbf{n}}\delta(\mathbf{x}-\mathbf{x}_f)ds + \rho\mathbf{g}\right). \tag{C.1}$$

Using continuity equation $\nabla \cdot \mathbf{u} = 0$ we obtain:

$$\nabla\cdot\left(-\frac{b^2}{12\mu}\nabla p\right) = \nabla\cdot\left(-\frac{b^2}{12\mu}\int_{\Gamma(t)} \sigma\kappa\hat{\mathbf{n}}\delta(\mathbf{x}-\mathbf{x}_f)ds + \rho\mathbf{g}\right). \tag{C.2}$$

Let us introduce the following reference values for the physical variables:

$$L_R = b; \qquad \mu_R = \mu_2;$$

$$p_R = \sigma/b; \quad U_R = \sigma/(12\mu_2);$$

$$\rho_R = \rho_2$$

If we follow the same adimensionalization procedure followed in 3.2 we obtain this system of non dimensional governing equations

NONDIMENSIONAL GOVERNING EQUATIONS

$$\begin{cases} \nabla^* \cdot \left(-\frac{1}{\mu^*} \nabla^* p^* \right) = -B \nabla^* \cdot \left(-\frac{1}{\mu^*} \rho^* \mathbf{j} \right) \\ \qquad\qquad + \nabla^* \cdot \left(-\frac{1}{\mu^*} \int \kappa^* \mathbf{n} \delta^* (\mathbf{x}^* - \mathbf{x}_f^*) ds^* \right) \\ \mathbf{u}^* = -\frac{1}{\mu^*} \left(\nabla^* p^* - \int \kappa^* \mathbf{n} \delta^* (\mathbf{x}^* - \mathbf{x}_f^*) ds^* + B \rho^* \mathbf{j} \right) \end{cases} \tag{C.3}$$

where B is defined as:

SURFACE TENSION/GRAVITY PARAMETER

$$B = \frac{b^2 \rho_2 g}{\sigma}$$

C.1.2 Boundary condition

Even if $\rho_1 = \rho_2$, the addition of gravity will introduce a hydrostatic pressure gradient that is linear in y. If we are computing on the rectangle $\Omega = [x_{min}, x_{max}] \times [y_{min}, y_{max}]$ and we set

$$\rho_0 = \frac{1}{L_x L_y} \int \int \rho(x, y) dx dy,$$

where $L_x = x_{max} - x_{min}$ and $L_y = y_{max} - y_{min}$, then we can write p as

$$p(x, y, t) = g \rho_0 (y_{max} - y) + \tilde{p}(x, y, t)$$

where $\tilde{p}$ is the deviation from the linear profile obtained from the average density ρ_0. If the boundaries are well away from the interface, then we expect $\tilde{p}$ to be roughly zero along the entire boundary $\partial\Omega$. The adimensional form of the boundary conditions is

NONDIMENSIONAL BOUNDARY CONDITIONS

$$p^*(y^*) = B \left(\frac{\rho_0}{\rho_2} \right) (y_{max}^* - y^*)$$

where

$$\frac{\rho_0}{\rho_2} = \frac{1}{L_x^* L_y^*} \int \int \rho^*(x, y) dx^* dy^*$$

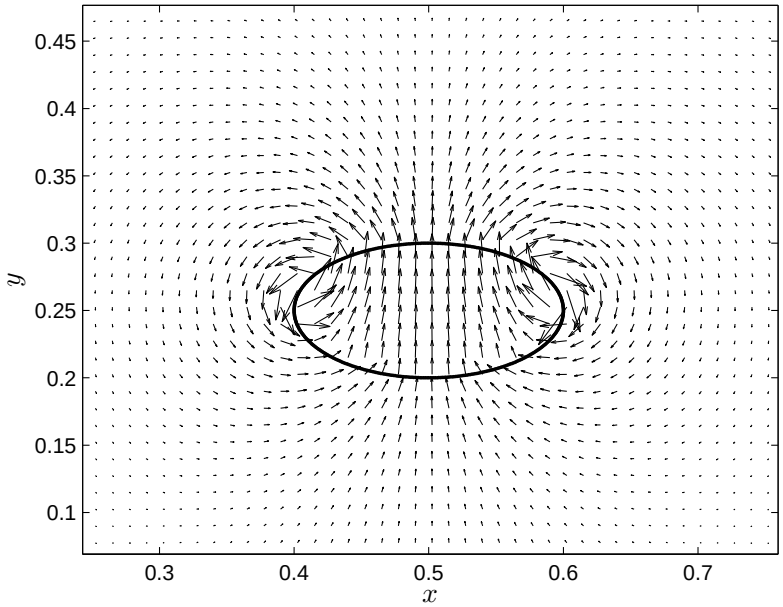

Figure 46: Velocity field, bubble rising

BIBLIOGRAPHY

[1] David Acheson. *Elementary Fluid Dynamics*. Oxford University Press, 1990 (cit. on p. 77).

[2] Lindner Anke et al. "Controlling Viscous Fingering". In: *Euro-Phys. News* (1999), pp. 77–78 (cit. on pp. vii, 4).

[3] J. Bataille. "Stabilitè d'un deplacement radial non-miscible". In: *Revue Inst. Petrole*. Vol. 23. 1968, pp. 1349–1364 (cit. on p. 16).

[4] George Keith Batchelor. *An Introduction to Fluid Dynamics*. New York: Cambridge University Press, 1967 (cit. on p. 77).

[5] David Bensimon et al. "Viscous Flows in Two Dimensions". In: *Rev. Modern Phys.* 58 (1986), pp. 977–999 (cit. on pp. vii, 4).

[6] R. L. Chuoke, P. van Meurs, and C. van der Pol. "The Instability of Slow Immiscible Viscous Liquid-Liquid Displacement in Permeable Media". In: *Petrol. Tran. AIME*. Vol. 216. 1959, pp. 188–194 (cit. on p. 16).

[7] Georges-Henri Cottet and Petros Komoutsakos. *Vortex Methods - Theory and Practice*. New York: Cambridge University Press, 2000 (cit. on pp. viii, 5).

[8] Yves Couder. "Viscous Fingering as an Archetype for Growth Patterns". In: *Perspectives in Fluid Dynamics*. Ed. by G. K. Batchelor, H. K. Moffatt, and M. G. Worster. Cambridge, 2000, pp. 53–98 (cit. on p. 11).

[9] *Enhanced Oil and Gas Recovery and Reservoir Characterization Research Group Web Site*. URL: http://www.ualberta.ca/tayfun/eogrrc/Overview.html/ (cit. on p. v).

[10] Petri Fast and Michael J. Shelley. "A moving overset grid method for interface dynamics applied to non-Newtonian Hele-Shaw flow". In: *J. Comput. Phys.* 195 (2003), pp. 117–142 (cit. on p. 13).

[11] Simone E. Hieber and Petros Koumoutsakos. "A Lagrangian Particle Level Set Method". In: *J. Comput. Phys.* 210 (2005), pp. 342–367 (cit. on pp. 46, 47).

[12] C. W. Hirt and B. D. Nichols. "Volume of Fluid (VoF) Method for the Dynamics of Free Boundaries". In: *J. Comput. Phys.* 39 (1981), pp. 201–225 (cit. on pp. viii, 5).

[13] George M. Homsy. "Viscous Fingering in Porous Media". In: *Ann. Rev. Fluid Mech.* 19 (1987), pp. 271–311 (cit. on pp. vii, 4).

[14] Thomas Y. Hou, John S. Lowengrub, and Michael J. Shelley. "Boundary Integral Methods for Multicomponent Fluids and Multiphase Materials". In: *J. Comput. Phys.* 169 (2001), p. 302 (cit. on pp. vii, 4, 54).

[15] Thomas Y. Hou, John S. Lowengrub, and Michael J. Shelley. "Removing the Stiffness from Interfacial Flows with Surface Tension". In: *J. Comput. Phys.* 114 (1994), pp. 312–338 (cit. on pp. 55, 56).

[16] Thomas Y. Hou et al. "A Hybrid Method for Moving Interface Problems with Application to the Hele-Shaw flow". In: *J. Comput. Phys.* 134 (1997), pp. 236–252 (cit. on p. 55).

[17] Eric Lajeunesse and Yves Couder. "On the Tip-Splitting Instability of Viscous Fingers". In: *J. Fluid Mech.* 419 (2000), pp. 125–149 (cit. on p. 55).

[18] Randall LeVeque and Li Zhilin. "Immersed Interface Methods for Stokes Flow with Elastic Boundaries or Surface Tension". In: *SIAM J. Sci. Comput.* 18 (1997), pp. 709–735 (cit. on p. 79).

[19] Shuwang Li, John S. Lowengrub, and Perry H. Leo. "A Rescaling Scheme with Application to the Long-Time Simulation of Viscous Fingering in a Hele-Shaw Cell". In: *J. Comput. Phys.* 225 (2007), pp. 554–567 (cit. on p. 55).

[20] Shuwang Li et al. "Control of Viscous Fingering Patterns in a Radial Hele-Shaw Cell". In: *Phys. Rev. Lett.* (2009) (cit. on pp. vii, 4).

[21] Lincoln Paterson. "Radial Fingering in a Hele-Shaw cell". In: *J. Fluid Mech.* 113 (1981), pp. 513–529 (cit. on pp. 18, 55).

[22] Charles S. Peskin. "Numerical Analysis of Blood Flow in the Heart". In: *J. Comput. Phys.* 25 (1977), p. 220 (cit. on p. 32).

[23] Charles S. Peskin and David M. McQueen. *A general method for the computer simulation of biological systems interacting with fluids*. Tech. rep. SEB Symposium on Biological Fluid Dynamics, 1994 (cit. on p. 33).

[24] Philip Geoffrey Saffman and Geoffrey Ingram Taylor. "The Penetration of a Fluid into a Porous Medium or Hele-Shaw Cell Containing a More Viscous Liquid". In: *Proceedings of the Royal Society of London, Mathematical and Physical Sciences*. Vol. 245. A 1242. 1958, pp. 312–329 (cit. on pp. 3, 8).

[25] James A. Sethian. "Evolution, Implementation, and Application of Level Set and Fast Marching Methods for Advancing Fronts". In: *J. Comput. Phys.* (2001) (cit. on pp. viii, 5).

[26] Seungwon Shin and Damir Juric. "Modeling Three-Dimensional Multiphase Flow Using a Level Contour Reconstruction Method for front Tracking without Connectivity". In: *J. Comput. Phys.* 180 (2002), pp. 427–470 (cit. on pp. viii, 5, 21, 23, 43, 47, 61).

[27] Paul Swarztrauber and Roland Sweet. "Efficient Fortran Subprograms for the Solution of Elliptic Equations". In: *ACM Transactions on Mathematical Software* 5 (1979), pp. 352–364 (cit. on p. 35).

[28] P. M. J. Trevelyan, C. Almarcha, and A. de Wit. "Buoyancy-driven Instabilities of Miscible Two-Layer Stratifications in Porous Media and Hele-Shaw Cells". In: *J. Fluid. Mech.* 670 (2011), pp. 38–65 (cit. on p. vii).

[29] Gretar Tryggvason and Hassan Aref. "Numerical Experiments on Hele-Shaw Flow with a Sharp Interface". In: *J. Fluid. Mech.* 136 (1983) (cit. on pp. 63, 64).

[30] Gretar Tryggvason et al. "A front-tracking method for computations of multiphase flow". In: *J. Comput Phys.* 169 (2001), p. 708 (cit. on pp. 21, 23, 36).

[31] Milton van Dyke. *An Album of Fluid Motion*. Parabolic Press, 1982 (cit. on p. 77).

[32] Henk van der Vorst. "Bi-CGSTAB: A Fast and Smoothly Converging Variant of Bi-CG for the Solution of Nonsymmetric Linear Systems". In: *SIAM Journal on Scientific and Statistical Computing* 13 (1992), pp. 631–644 (cit. on p. 40).

[33] Norman J. Zabusky, M. H. Hughes, and K. V. Roberts. "Contour Dynamics for the Euler Equations in Two Dimensions". In: *J. Comput. Phys.* 135 (1997), pp. 96–106 (cit. on pp. viii, 5).

[34] Jianhua Zhang, Jun Luo, and Zhenhua Liu. "DLA Simulation with Stricking Probability for Viscous Fingering". In: *Consumer Electronics, Communications and Networks (CECNet)*. 2011, pp. 4044–4047 (cit. on p. 59).